NUCLEAR DATA AND MEASUREMENTS SERIES

ANL/NDM-133

Fast-Neutron Scattering at Z = 50: Tin

by

A.B. Smith

August 1994

ARGONNE NATIONAL LABORATORY,
ARGONNE, ILLINOIS 60439, U.S.A.

NUCLEAR DATA AND MEASUREMENTS SERIES

ANL/NDM-133

FAST-NEUTRON SCATTERING AT Z = 50:- TIN

A. B. Smith
August, 1994

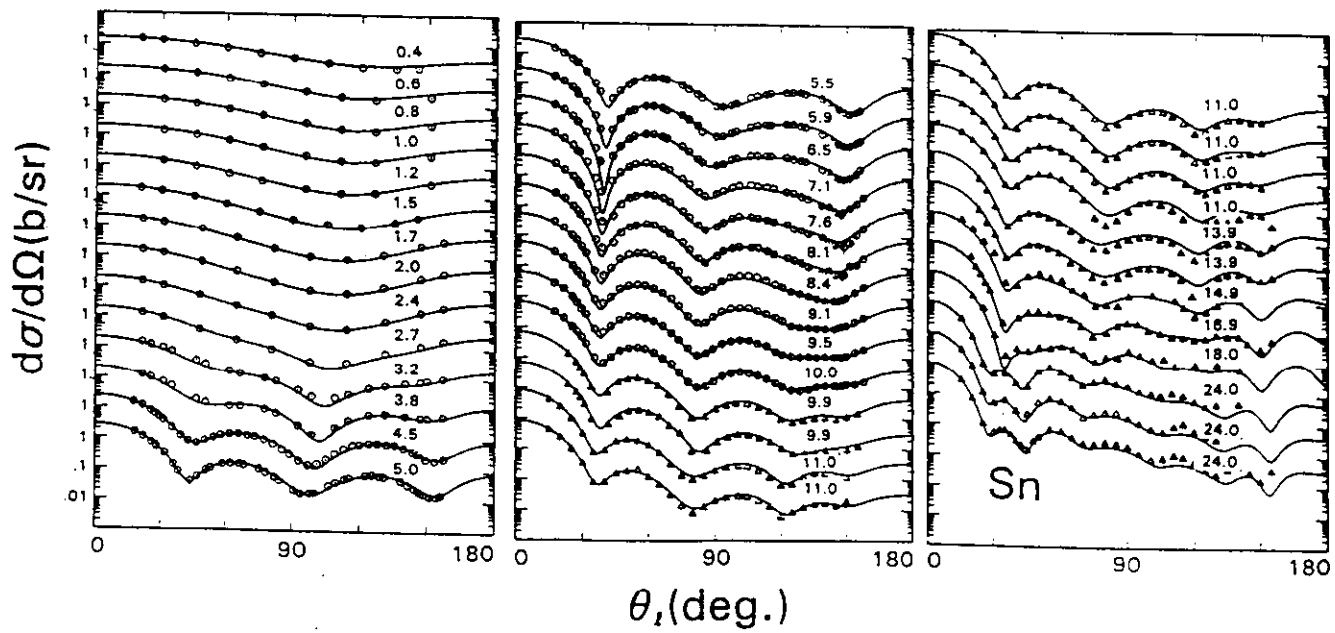

ARGONNE NATIONAL LABORATORY, ARGONNE, ILLINOIS

Operated by THE UNIVERSITY OF CHICAGO
for the U. S. DEPARTMENT OF ENERGY
under Contract W-31-109-Eng-38

Argonne National Laboratory, with facilities in the states of Illinois and Idaho, is owned by the United States government, and operated by The University of Chicago under the provisions of a contract with the Department of Energy.

Reproduced from the best available copy.

Available to DOE and DOE contractors from the
Office of Scientific and Technical Information
P.O. Box 62
Oak Ridge, TN 37831
Prices available from (615) 576-8401

Available to the public from the
National Technical Information Service
U.S. Department of Commerce
5285 Port Royal Road
Springfield, VA 22161

ANL/NDM-133

FAST-NEUTRON SCATTERING AT Z = 50:- TIN*

by

A. B. Smith

Argonne National Laboratory
Argonne, Illinois
and
The University of Arizona
Tucson, Arizona

August, 1994

Keywords:-
Measured σ_t (0.8-4.5 MeV), and $d\sigma/d\Omega_{el}$ and $d\sigma/d\Omega_{inel}$ (1.5-10 MeV) for neutrons incident on elemental tin. Model interpretations.

---

* This work supported by the United States Department of Energy under contract W-31-109-Eng-38, and by the Department of Nuclear and Energy Engineering, College of Engineering and Mines, University of Arizona.

PUBLICATIONS IN THE ANL/NDM SERIES

A listing of recent issues in this series is given below. Issues and/or titles prior to ANL/NDM-116 can be obtained from the National Technical Information Service, U. S. Department of Commerce, 5285 Port Royal Road, Springfield, VA 22161, or by contacting the author of this report at the following address:-

Technology Development Division
Argonne National Laboratory
9700 South Cass Avenue
Argonne, IL 60439
USA

S. CHIBA, P.T. GUENTHER, R.D. LAWSON, AND A.B. SMITH
Neutron Scattering from Elemental Indium, the Optical Model, and the Bound-State Potential
ANL/NDM-116, June 1990

D.L. SMITH AND L.P. GERALDO
An Evaluation of the Nb-93(n,n')Nb-93m Dosimeter Reaction for ENDF/B-VI
ANL/NDM-117 (November 1990)

J.W. MEADOWS
Characteristics of the Samples in the FNG Fission Deposit Collection
ANL/NDM-118 (November 1990)

S. CHIBA, P.T. GUENTHER, A.B. SMITH, M. SUGIMOTO, AND R.D. LAWSON
Fast-Neutron Interaction with Elemental Zirconium, and the Dispersive Optical Model
ANL/NDM-119, June 1991

A.B. SMITH, P.T. GUENTHER, J.F. WHALEN, AND S. CHIBA
Fast-neutron Total and Scattering Cross Sections of ^{58}Ni and Nuclear Models
ANL/NDM-120, July 1991

S. CHIBA AND D.L. SMITH
A Suggested Procedure for Resolving an Anomaly in Least-squares Data Analysis Known as "Peelle's Pertinent Puzzle" and the General Implications for Nuclear Data Evaluation
ANL/NDM-121, September 1991

D.L. SMITH AND DOMINIQUE FEAUTRIER
Development and Testing of a Deuterium Gas Target Assembly for Neutron Production Via the H-2(D,N)HE-3 Reaction at a Low-energy Accelerator Facility
ANL/NDM-122, March 1992

D.L. SMITH AND E.T. CHENG
A Review of Nuclear Data Needs and Their Status for Fusion Reactor Technology with some Suggestions on a Strategy to Satisfy the Requirements
ANL/NDM-123, September 1991

J.W. MEADOWS
The Thick-Target $^{9}Be(d,n)$ Neutron Spectra for Deuteron Energies Between 2.6 and 7.0-MeV
ANL/NDM-124, November 1991

A.B. SMITH AND P.T. GUENTHER
Fast-Neutron Scattering Near Shell Closures:- Scandium
ANL/NDM-125, August 1992

A.B. SMITH, J.W. MEADOWS AND R.J. HOWERTON
A Basic Evaluated Neutronic Data File for Elemental Scandium
ANL/NDM-126, November 1992

A.B. SMITH AND P.T. GUENTHER
Fast-Neutron Interaction With Vibrational Cadmium Nuclei
ANL/NDM-127, November 1992

D.L. SMITH
A Least-Squares Computational "Tool Kit"
ANL/NDM-128, April 1993

JOSEPH McCABE, A.B. SMITH AND J.W. MEADOWS
Evaluated Nuclear Data Files for the Naturally-Occurring Isotopes of Cadmium
ANL/NDM-129, June 1993

A.B. SMITH AND P.T. GUENTHER
Fast-Neutron Interaction with the Fission Product ^{103}Rh
ANL/NDM-130, September 1993

A.B. SMITH AND P.T. GUENTHER
Fast-Neutron Scattering from Vibrational Palladium Nuclei
ANL/NDM-131, October 1993

A.B. SMITH
Neutron Interaction with Doubly-Magic ^{40}Ca
ANL/NDM-132, December 1993

TABLE OF CONTENTS

ANL/NDM-133

FAST-NEUTRON SCATTERING AT Z = 50:- TIN

by

A. B. Smith

Argonne National Laboratory
Argonne, Illinois
and
The University of Arizona
Tucson, Arizona

ABSTRACT

Neutron total cross sections of elemental tin were measured from ≈ 0.8 to 4.5 MeV with energy detail sufficient to average intermediate structure. Neutron elastic- and inelastic-scattering cross sections were measured from ≈ 1.5 to 10 MeV. Below 3 MeV 10 angular intervals were used distributed between ≈ $20^{o}$and 160^{o}, and the incident energy increments were ≈ 0.1 MeV. From 3 to 4 MeV twenty angular intervals, distributed over the same angular range, were used, and the energy increments were ≈ 0.2 MeV. From 4.5 to 10 MeV the measurements were made at ≥ 40 angular intervals distributed between ≈ 17^{o} and 160^{o}, and at energy increments of ≈ 0.5 MeV. Inelastic neutron groups corresponding to average excitations of approximately 1.15 and 2.27 MeV were observed. The experimental results were combined with elemental and isotopic values available in the literature, extending from ≈ 0.4 to 24 MeV, to form a comprehensive data base for physical interpretations using optical-statistical, dispersive-optical and coupled-channels models. The parameters of the models were determined in detail, including isospin, and collective effects. These physical interpretations were compared with present and previously-reported experimental results and with theoretical physical concepts.

1. Introduction

Tin is an unusual element. It is magic in proton number with ten isotopes, approximately 83% of which are even spanning the mass range 112 to 124, and nearly 82% of the isotopic abundance is concentrated in the five even isotopes ^{116,118,120,122} and ^{124}Sn. The latter isotopes have similar excited structure characterized by one- and two-phonon quadrupole vibrational levels and a low-lying 3^- octupole vibrational level [NDS]. The quadrupole deformation parameter, β_2, is relatively small (≈ 0.11), and the isotopes are generally considered to be nearly spherical with relatively weak quadrupole and octupole vibrations. These properties make the tin isotopes attractive for studies of asymmetry (i.e. isospin) and collective effects. Indeed, there have been a number of (p,p) studies of the interaction with the tin isotopes (e.g., [Bee+70], [BG68] and [Mak+68]) and a few (p,n) studies (e.g., [Won+84]) resulting in a variety of isoscaler and isovector potentials, often with quite different geometric parameters. The complimentary neutron interactions have been less studied. There are recent high-quality results from $\approx$ 10 to 25 MeV ([Gus+89], [Chi+88], [Rap+80] and [Fin+80A]), but only very limited information at lower energies ([SH67] and [Har+84]). The latter region is where dispersive effects will be most evident and where it has been suggested that there are rather sharp changes in potential parameters if the very low strength functions are to be reasonably accounted for ([MN82], [Gus+89] and [NDC72]). The physical interpretations of the neutron-scattering results are based upon the optical model, DWBA methods and, in one case, coupled-channels calculations. There has been no consideration of dispersive effects. The physical results are generally based on measurements made at a single or few incident energies thus energy dependence of the potentials is uncertain. Some of the reported isospin and collective effects vary by large amounts. There are only a few measurements of inelastic scattering from either the element or the isotopes below $\approx$ 10 MeV (e.g., [Gus+89] and [Tan+71]). Clearly, the neutron scattering processes are uncertain below $\approx$ 10 MeV, and even at higher energies the reported data is not always consistent. The prior data base and interpretations are at least deficient at the lower energies and not all that consistent at higher energies.

The tin isotopes are fission products and thus their fundamental nuclear properties are a concern in nuclear-energy development, particularly in fuel-cycle and incineration considerations. Moreover, it is known [ENDF] that contemporary evaluated tin fission-product nuclear-data files do not well represent experimental understanding, even of the total cross section, above several-100 keV. Thus they have shortcomings when used to evaluated FBR-incineration concepts, such as the Integral Fast Reactor [TC88], or spallation-source incineration.

The present study was undertaken to address some of fundamental questions cited above, and also to provide a sound basis for the derivation of evaluated nuclear-data files for nuclear-energy

applications. Section 2 of the following very briefly outlines the experimental methods employed. Section 3 presents the experimental results. Section 4 describes an extensive development of relevant nuclear models. And finally, Section 5 discusses and summarizes the measured and calculated results and makes comparisons with previously reported information.

2. Experimental Methods

The total-cross-section measurements were carried out using the conventional transmission technique. The samples were cylinders of elemental metallic tin, alternatively 2 cm in diameter and 2 cm long or 2.5 cm long and 2.5 cm in diameter. The neutron source was the $^{7}Li(p,n)^{7}Be$ reaction [Dro87] with the incident proton beam pulsed at a repetition rate of 2 MHz and a burst duration of ≈ 1 nsec. The lithium of the target was deposited in metal form to a thickness providing neutron energy spreads at the sample of ≈ 50 keV. The mean energy of the neutron burst was determined to ≈ 10 keV by magnetic analysis of the incident proton beam. A massive collimator defined a neutron beam of ≈ 1 cm diameter at a zero-degree reaction angle. The transmission samples were placed upon a wheel ≈ 280 cm from the neutron source at the exit of the collimator, with the beam incident upon the cylindrical bases of the samples. The sample wheel was rotated in a stepping motion, changing the samples approximately every five seconds. In addition to the tin samples, the wheel held "voids" for determining the incident beam intensity and carbon reference samples for verification purposes. With the rapid rotation of the sample wheel through many cycles, source-intensity fluctuations were averaged out and no independent source-intensity monitoring was required. The neutron detector consisted of a 12 cm diameter and 2 cm thick liquid scintillator centered on the neutron-beam axis ≈ 3 m from the sample. Conventional time-of-flight techniques were used to separate neutrons of the burst from the small time-uncorrelated background and to resolve contributions from the primary and secondary neutron groups from the source reaction. The data was accumulated and reduced to cross sections on-line using a digital computer. The circuitry was arranged to contain a random test signal for explicit dead-time corrections. In-scattering corrections were estimated and found to be negligible. No self-shielding corrections were made but results obtained with the two different-sized samples were consistent. These total-cross-section measurement techniques have been extensively reported elsewhere [PWS81].

All of the neutron scattering measurements were made using the time-of-flight technique [CL55]. Below 4 MeV the $^{7}Li(p,n)^{7}Be$ reaction was used as a neutron source with a neutron energy spread of ≈ 50 keV at the scattering sample. Above 4 MeV the $D(d,n)^{3}H$ reaction was used as the source [Dro87] with the deuterium contained in a gas cell at pressures providing incident-neutron spreads at the sample of ≈ 300 keV at 4.5 MeV, decreasing to ≈ 100 keV at 10 MeV. Both sources were pulsed at a 2 MHz repetition rate with a burst duration of ≈ 1 nsec. The mean neutron energy at the sample was again determined to within

≈ 10 keV by magnetic analysis of the incident ion beam. The scattering sample was the smaller of the two samples defined above, placed ≈ 18 cm from the source at a zero-degree reaction angle. Ten ≈ 5 m flight paths were distributed about the sample. The relative scattering angles were optically determined to better than 0.1^{0} and their normalization determined to better than 0.25^{0} by the observation of highly anisotropic elastic scattering at either side of the center line. The neutron detectors were 12.5 cm diameter liquid scintillators with γ-ray suppression pulse-shape discrimination. Below 4 MeV they were 2 cm thick and above 4 MeV 6 cm thick. Their relative energy dependence was determined by the observation of neutrons emitted at the fission of ^{252}Cf in the manner described in ref. [SGS77], and the absolute normalization determined by the measurement of elastic scattering from carbon at energies of ≤ 4 MeV, or from H(n,n) scattering above 4 MeV [CSL83]. The measured time spectra were reduced to cross sections and corrected for angular resolution, sample attenuation and multiple-even effects using Monte-Carlo methods [Smi90]. These scattering-measurement procedures have been successfully used for many years and are extensively described elsewhere [Smi+92].

3. Experimental Results

3.1. Neutron Total Cross Sections

The total cross sections were measured from ≈ 0.8 to 4.5 MeV. Several passes were made over this energy range in steps of ≈ 10 keV. The results were consistent, and were combined and averaged over 50 keV energy increments. The total estimated cross-section uncertainties were ≈ 1.5 → 3%, about half of which was systematic due primarily to background effects. These results are the most detailed available over the relevant energy range. They compare favorably with similar averages of elemental total cross sections reported in the literature ([PW83], [MW66], [FG71], [Rap+80], [LHH81], [Fin+93]) as illustrated in Fig. 3.1.1. Over the energy range of the present measurements the energy-averaged total cross sections of elemental tin appear known to <≈ 2%. A more detailed description of these results is given in the preliminary laboratory report of ref. [BGS82].

3.2. Neutron Elastic Scattering Cross Sections

The elastic-scattering measurements were made with sufficient scattered-neutron resolution to separate the elastic contribution from the inelastic component due to the excitation of the yrast (2^{+}) states of the even isotopes. The inelastic-scattering contribution due to the excitation of the first few excited states in the odd isotopes (≈ 16% abundant) was not resolved from the elastic scattering. What is reported here as "elastic" scattering is inclusive of this odd-isotope inelastic contribution. This small perturbation is explicitly dealt with in the model derivations discussed below.

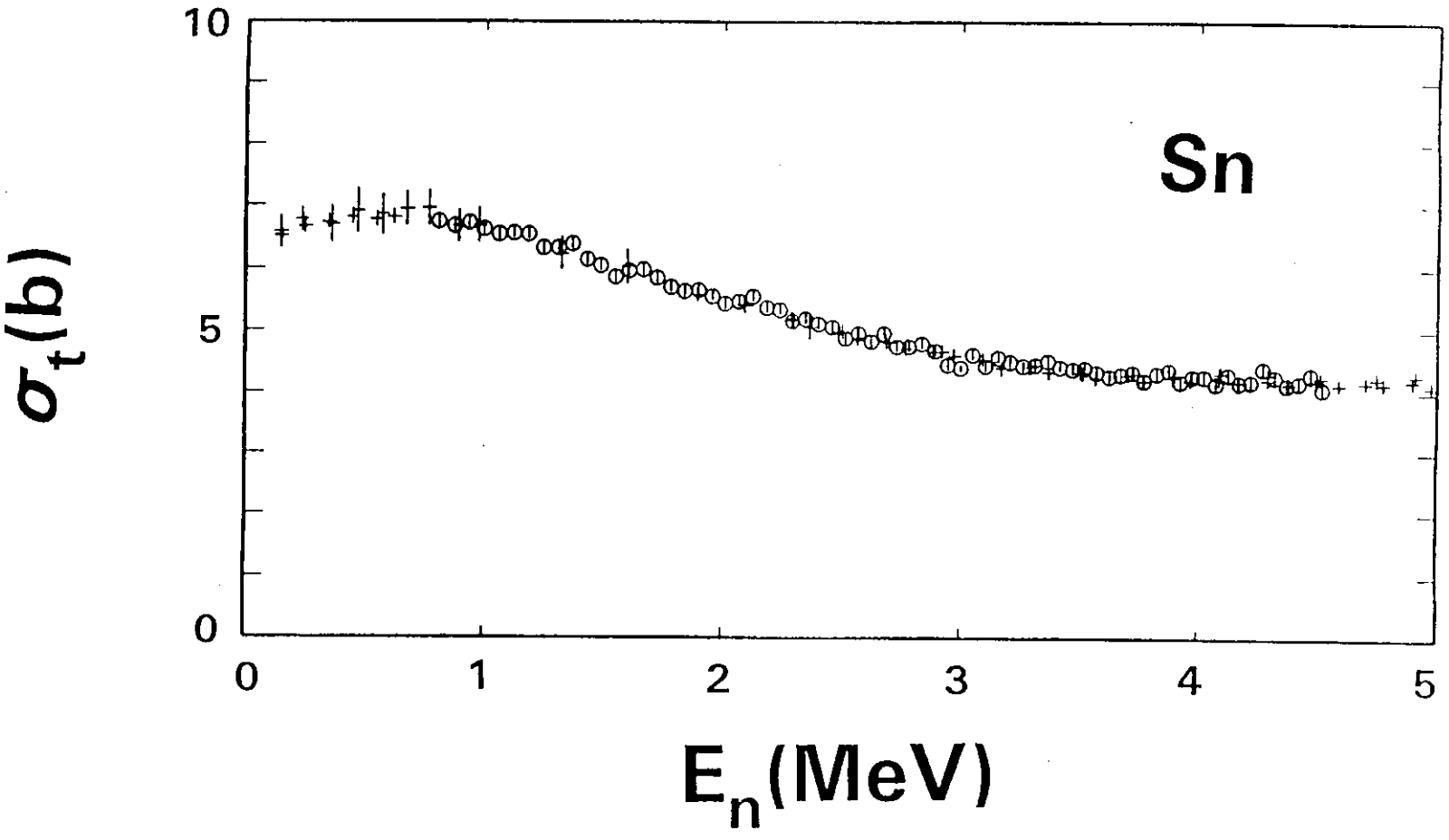

Fig. 3.1.1. Comparison of the present measured elemental tin total cross sections (circular symbols) with similar energy averages of values reported in the literature (+ symbols).

From 1.5 → 3 MeV the elastics-scattering measurements were made in ≈ 100 keV steps and at ten scattering angles distributed between ≈ 20^{o} and 160^{o}. From 3 → 4 MeV the measurements were made at ≈ 200 keV intervals and twenty angles distributed over the same angular range. The estimated uncertainties associated with these lower-energy differential values are ≈ 5%. The lower-energy results are illustrated in Fig. 3.2.1. A preliminary version of these results is given in the laboratory report of ref. [BGS82].

From 4.5 → 10 MeV elastic-scattering measurements were made at incident-energy intervals of ≈ 0.5 MeV and at ≥ 40 scattering angles distributed between ≈ 17^{o} and 160^{o}. The uncertainties in the differential values ranged from 3% to larger amounts in the minima of the distributions, including statistical, systematic and angle-uncertainty contributions. These higher-energy results are illustrated in the 4.5 → 10 MeV portion of Fig. 3.2.2.

There are surprisingly few comprehensive elemental tin elastic-scattering results comparable with present values reported in the literature. At the lower energies of the present work there is good agreement with the ^{120}Sn results of Tanaka et al. [Tan+71]. Near 10 MeV the present results are consistent with the ^{116} and ^{120}Sn results of Guss et al. [Gus+89]. The experimental data in the literature in a broader context is discussed in Section 4.1.

3.3. Neutron Inelastic Scattering

Some elemental inelastic-scattering cross sections were determined at incident energies up to ≈ 10 MeV in concert with the elastic-scattering measurements. These results correspond to observed excitations dispersed about ≈ 1.15 and ≈ 2.27 MeV. The first group was attributed to the excitation of yrast (2^{+}) one-phonon vibrational states of the even isotopes which are closely bunched over a narrow energy range of ≈ ± 100 keV [NDS]. In addition, there will be a number of contributions from the odd isotopes, but their collective isotopic abundance is only ≈ 16%. The second observed inelastic-neutron group was attributed to two-phonon-quadrupole and octupole vibrational states in the even isotopes with additional contributions from the even isotopes, and from a number of levels in the minor odd isotopes. The experimental resolution was not sufficient to separate the individual isotopic components of either group, and thus the cross sections reported here are elemental averages of the isotopic contributions. They should approach averages of the even-isotopic contributions. Both of the observed inelastically-scattered neutron groups were anisotropically distributed, increasingly so with energy above ≈ 5 MeV as is expected from significant direct-reaction contributions. This behavior is illustrated in Fig. 3.3.1. The corresponding angle-integrated cross sections were determined by fitting the experimental differential

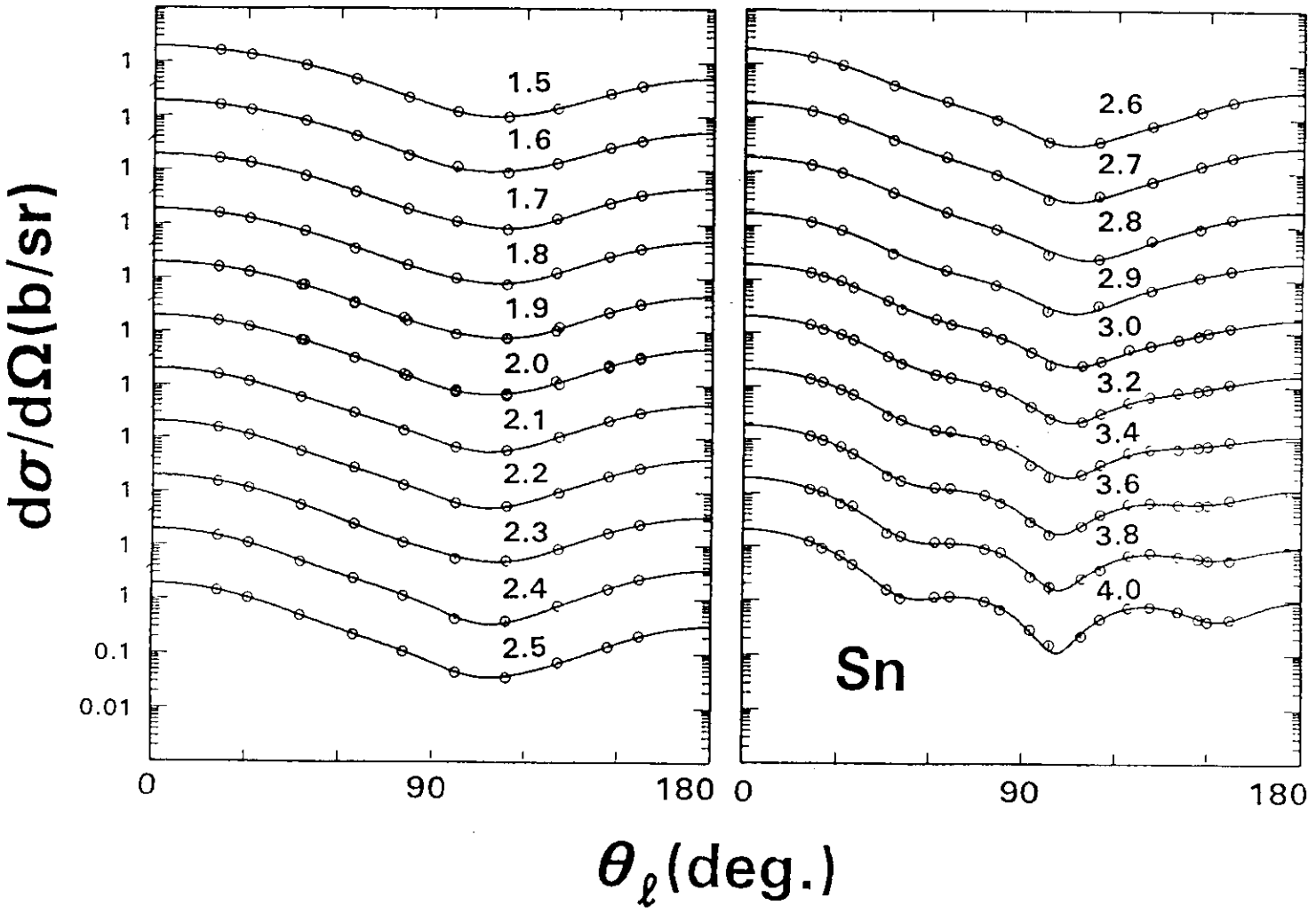

Fig. 3.2.1. Measured elemental tin elastic-scattering cross sections from 1.5 → 4 MeV (symbols). Curves represent Legendre polynomial fits to the data. Approximate incident energies are numerically given in MeV. Throughout this report data is shown in the laboratory coordinate system.

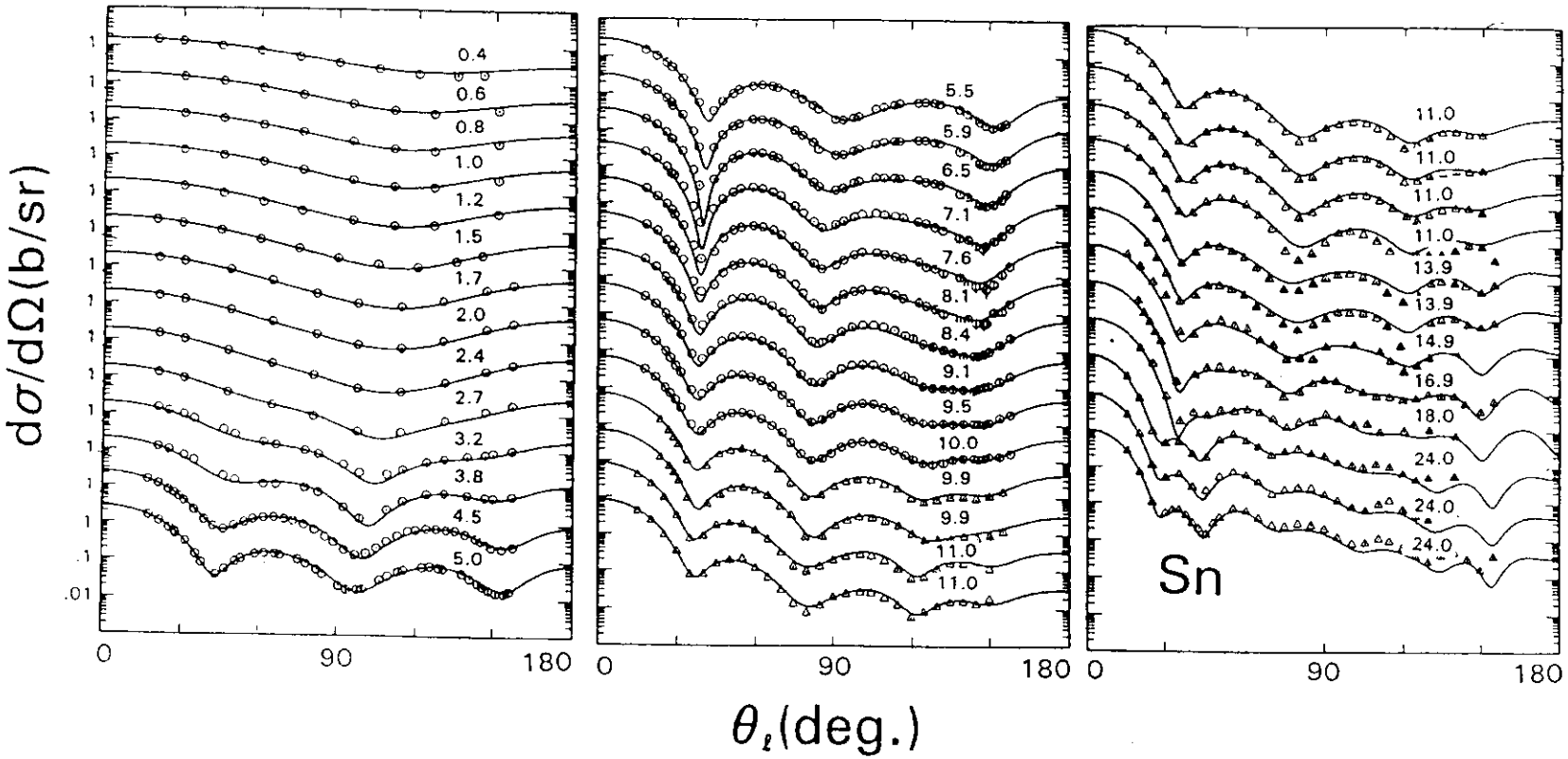

Fig. 3.2.2. Measured (symbols) and calculated (curve) elastic-scattering cross sections of tin. The circular symbols are the elemental values from this laboratory including the results of the present work. The Δ symbols denote the isotopic experimental values of the data base as discussed in Section 4.1. The calculations employed the ESOM of Table 4.3.3. Approximate incident energies are numerically noted in MeV.

distributions with Legendre-polynomial series. The resulting elemental angle-integrated cross sections, with their estimated uncertainties, are illustrated and compared with the few available values reported in the literature in Fig. 3.3.2.

Many of the tin inelastic-scattering results reported in the literature are isotopic values not directly comparable with the present elemental results, and generally at higher incident energies. However, the 10 MeV ^{116} and ^{120}Sn inelastic-scattering angular distributions of ref. [Gus+89] are very consistent with the present 10 MeV elemental results. The detailed nature of the higher-energy differential isotopic inelastic-scattering cross sections is discussed in Section 5.

4. Physical Models

4.1. Data Base

The primary basis for the model derivations was the differential elastic-scattering distributions. These were obtained as follows:- i) Below ≈ 1.5 MeV the very early elemental work of the author and associates was used [SH67]. These distributions were averaged over ≈ 200 keV incident-energy intervals in order to smooth any physical fluctuations and to reduce the data base to manageable proportions. ii) From ≈ 1.5 → 4.0 MeV the results of the present work were used. These were somewhat augmented with the ^{120}Sn results of Tanaka et al. [Tan+71], and the combined data averaged over ≈ 300 keV intervals. iii) From ≈ 4.5 → 10 MeV the results of the present work were used. iv) Above ≈ 9.9 MeV, continuing to a maximum of 24 MeV, a number of isotopic distributions were taken from the literature ([Gus+89], [Rap+80], [Fer+77], [Chi+88]). All of the previously-reported data is available at the National Nuclear Data Center in numerical form. The elastic-scattering data base is illustrated in Fig. 3.2.2.

Secondary attention was given to neutron total cross sections, strength functions, scattered-neutron polarizations and inelastic scattering. The elemental total cross sections were constructed from the present results and those given in the literature ([FG71], [MW66], [PW83], [LHH81], [Fin+93]). In order to smooth any lower-energy fluctuations, and to reduce the large number of numerical values to manageable proportions, the total cross sections were averaged over ≈ 100 keV to 1 MeV, over ≈ 200 keV from 1 ≈ 5 MeV and over ≈ 500 keV above 5 MeV. This total-cross-section data base is illustrated in Fig. 4.1.1. Strength functions were taken from refs. [MDH81], [PS86] and [Nak+86]. The inelastic-scattering data was taken from the present work and from isotopic results reported in the literature ([Tan+72], [Gus+89], [Chi+88], [Ste+65], [Fin+80A]). Scattered-neutron polarizations were taken from ref. [Gus+89].

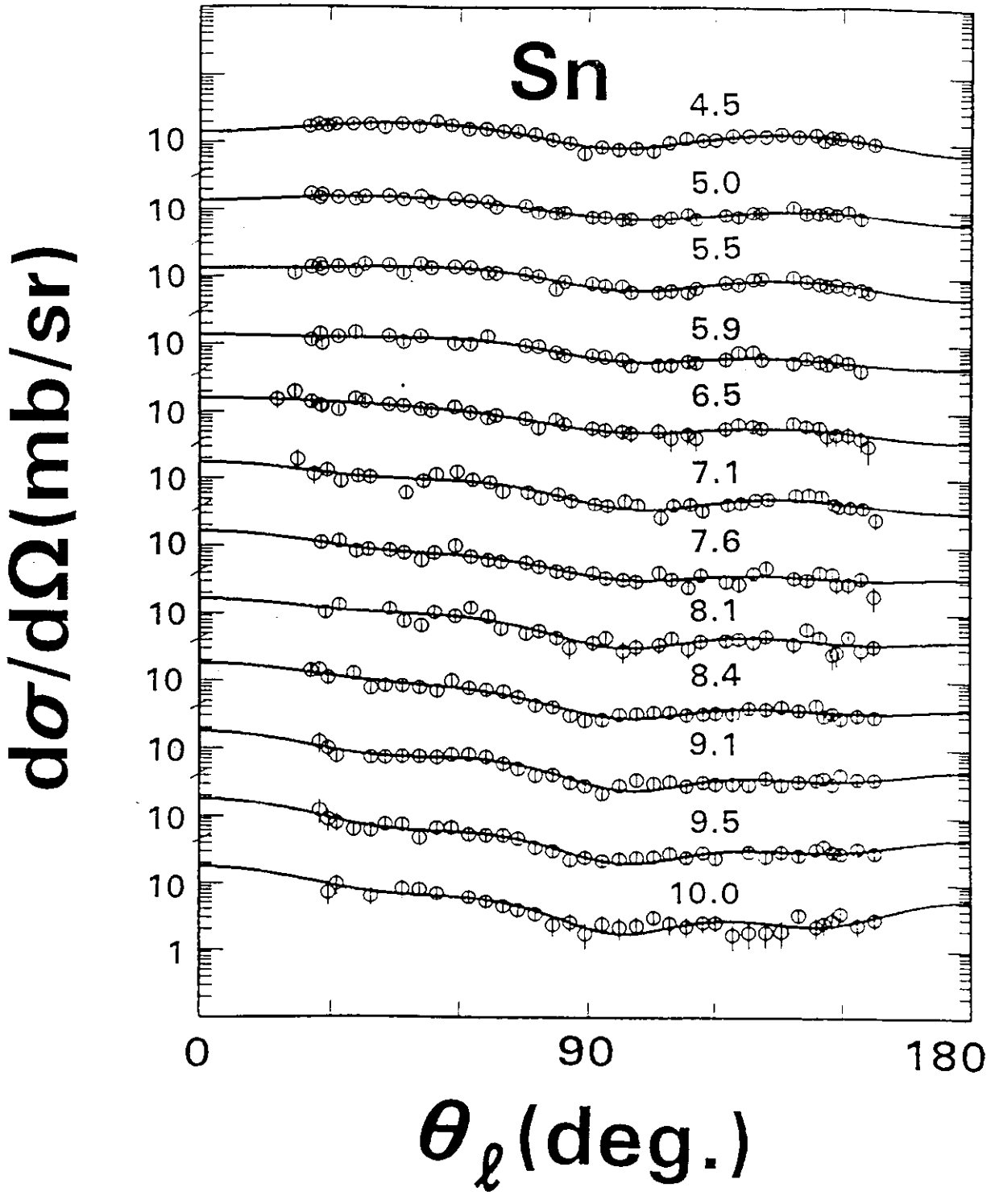

Fig. 3.3.1. Differential elemental inelastic-scattering cross sections resulting from mean excitations of ≈ 1.15 MeV. The present experimental results are indicated by symbols, and curves are "eyeguides" obtained by Legendre-polynomial fitting. Approximate incident-neutron energies are numerically noted.

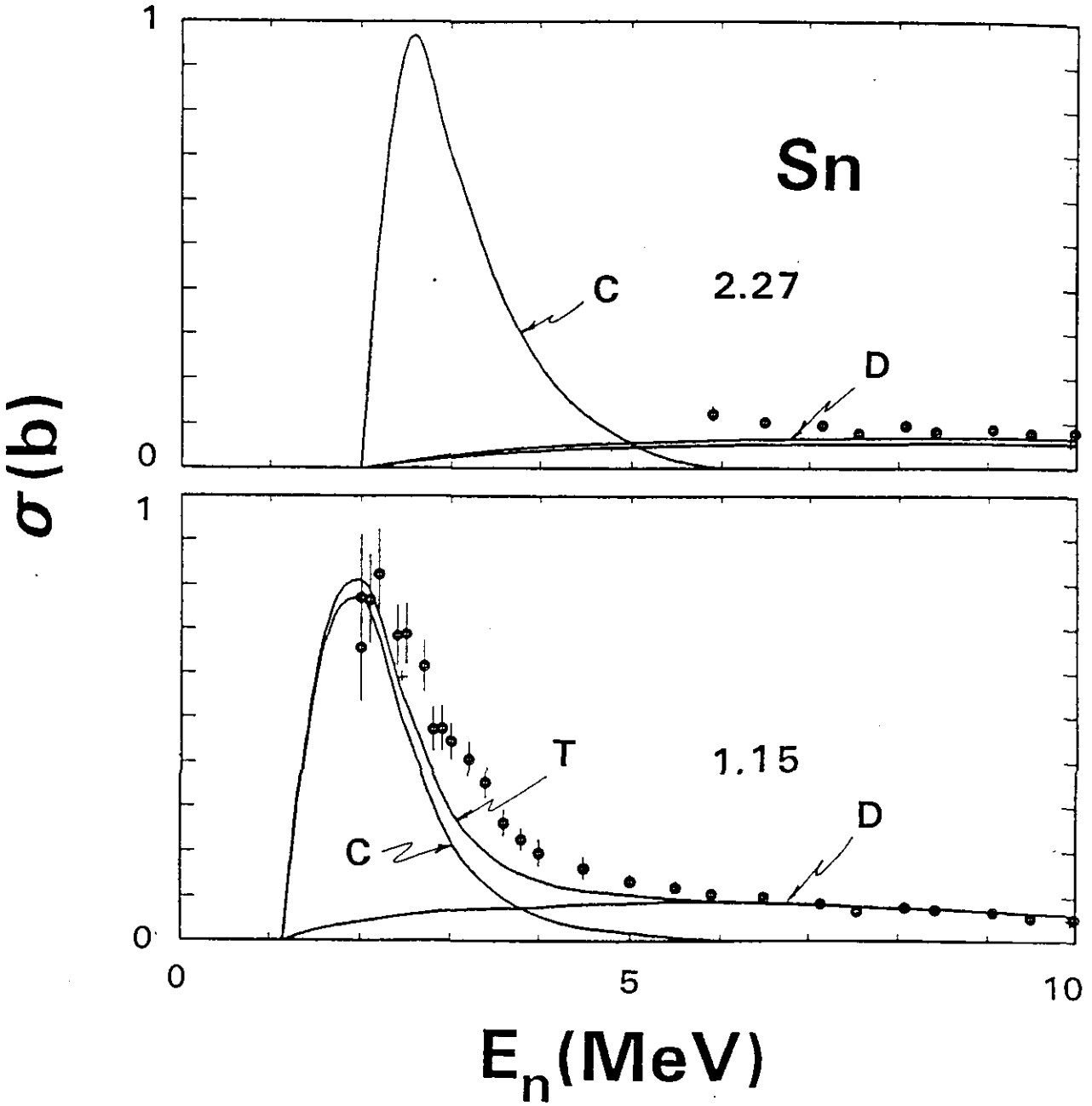

Fig. 3.3.2. Angle-integrated inelastic-scattering cross sections of tin. The present experimental results are indicated by concentric circular symbols, and those from the literature ([Gus+89], [CL56]) by "+" symbols. The "C" curve represents CN results calculated with the ESOM, the "D" curve direct-reaction contributions calculated with the CCM and curve T = C + D. The observed excitation energies are numerically cited in MeV.

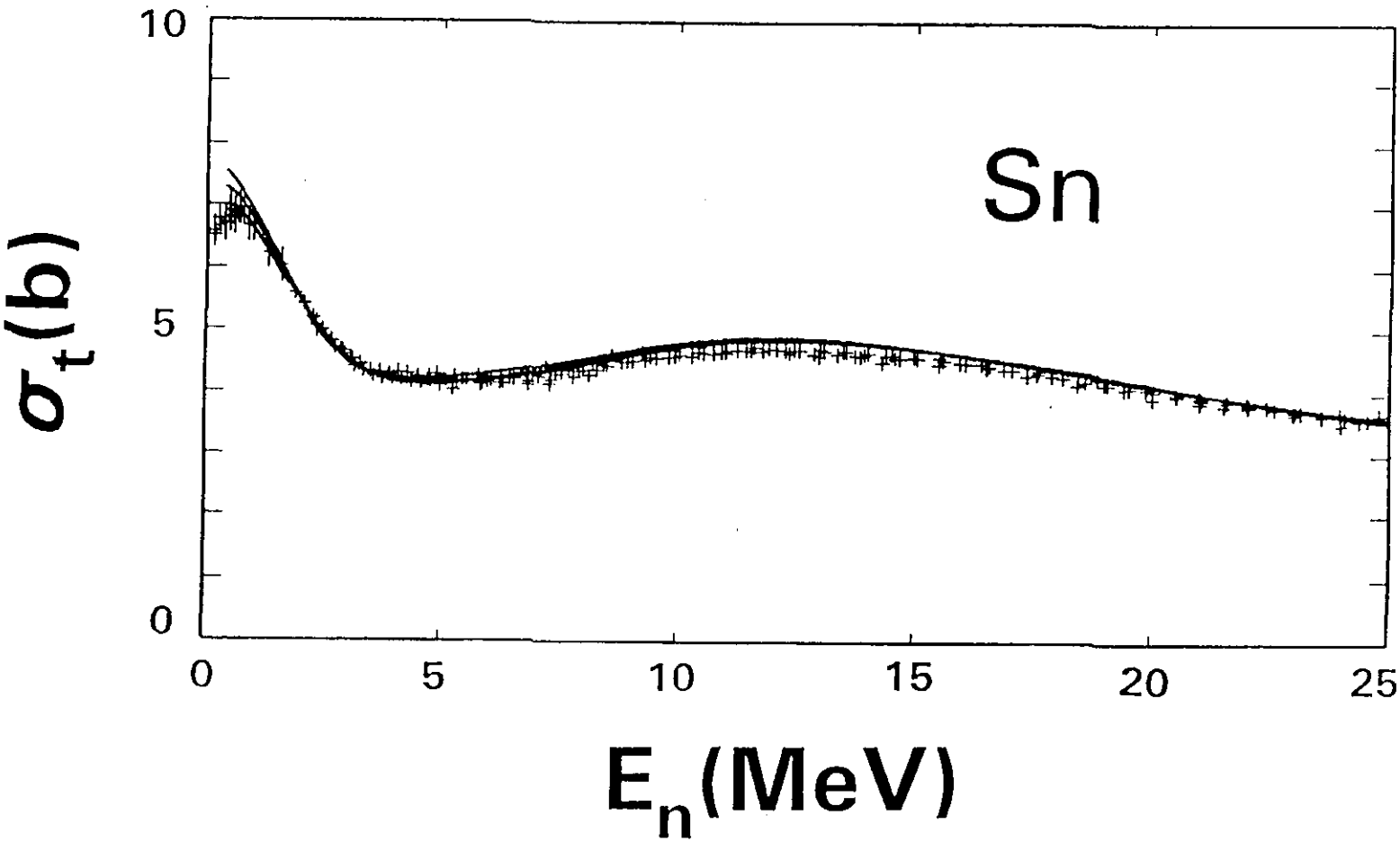

Fig. 4.1.1. Energy averages of elemental tin neutron total cross sections (symbols) and model-calculated values (curves). The three curves were obtained with the ESOM, DOM and CCM discussed in the text. They are indistinguishable except at very low energies where the DOM result is lowest and the CCM result highest.

4.2. Potential Forms

All of the physical modeling assumed: i) a real potential of the Saxon-Woods (SW) form, ii) a surface-absorption potential of the SW-derivative form, and iii) a spin-orbit potential of the Thomas form [Hod71]. (Throughout, the spin-orbit potential parameters of ref. [WG86] were used.) Where a volume absorption was considered that potential was assumed to have the SW form with the geometries of the real potential.

4.3. The Spherical Optical Model (SOM)

The spherical optical models were deduced from the elastic-scattering data base by chi-square fitting following the five-step procedure employed by the author in a number of previous investigations [Smi+92]. These steps were:- i) Six parameter fitting varying real- and imaginary-potential strengths, radii and diffusenesses. From this the real-potential diffuseness, a_v, was fixed. Experience has shown it to be of a generally "global" nature not perturbed by nuclear structure. ii) With a_v fixed, five-parameter fits were used to determined the real radius, r_v. iii) Four parameter fits (with a_v and r_v fixed) were then used to determine the imaginary-potential radius, r_w. iv) Three parameter fits determined the imaginary-potential diffuseness, a_w. Finally, v) two parameter fitting, with the geometries fixed to the prior-selected values, determined the real- and imaginary-potential strengths. These were expressed in terms of volume-integrals-per-nucleon as a number of the geometric parameters were energy dependent. This five-step procedure is sensitive to the well-known correlations of real strength and radius and of imaginary strength and diffuseness, but the sample is large and thus variations due to such correlations should be averaged out. On the other hand, the procedure is not constrained to assumed parameter regions as occurs when the initial fitting is limited to a few parameters (usually potential strengths) and then widened to a larger parameter space in successive steps.

All of the SOM calculations were carried out with the computer code ABAREX [Mol82]. At energies above 8 MeV, it was assumed that the elastic scattering was entirely due to shape-elastic (SE) processes. At lower energies the compound-nucleus processes (CN) were considered in detail as defined below. The level energies, spins and parities were taken from the Nuclear Data Sheets [NDS] up to excitations of $\approx$ 2 MeV. Higher-energy excitations were represented by the statistical formalism of Gilbert and Cameron [GC65]. The CN contributions were calculated with the Hauser-Feshbach formula [HF52], modified to include resonance fluctuation and correlation effects in the manner described by Moldauer [Mol80].

Initially, an approximate SOM was determined assuming that the data base consisted entirely of a single isotope with the elemental

mass of 118.7 and the excited level structure of ^{118}Sn. Herein, this first approximation is identified as the "isotopic spherical optical model", or ISOM. These assumptions ignore the odd isotopes, which can effect the low-energy calculations, and the isotopic nature of the data base above ≈ 10 MeV. The neglect of the odd isotopes should be a minor perturbation as they are only 16% abundant, and the excited structure of the even isotopes is similar. The isotopic data at higher energies generally tends to span the even isotopes so, on the average, is reasonably approximated by the above assumptions, although, of course, no consideration is given to the potential dependence on the asymmetry, (N-Z)/A. With these caveats, the potential of Table 4.3.1 was obtained. The potential reasonably describes the data base from which it was developed and the experimental total cross sections, giving a result essentially equivalent to that obtained with the more detailed ESOM described below. The strength functions calculated with the ISOM are given in Table 4.3.2.

The above approximate ISOM was refined to explicitly include the isotopic nature of the data base. The elemental data were assumed to consist of the six isotopes $^{116\text{-}122}$Sn with the relative abundances normalized to 100%. These isotopes are 92.2% of the element. The isotopic distributions of the data base, generally above 10 MeV, were treated as the respective isotopes. This more detailed description is termed the "elemental spherical optical model", or ESOM, herein. The level structure of each isotope was explicitly treated using the energies, spins and parities given in the Nuclear Data Sheets [NDS], and continuum level properties were taken from the statistical representation of Gilbert and Cameron [GC65]. The calculations combined the elastic and first two inelastic groups groups in the odd isotopes so as to be consistent with the experimental resolutions. The $A^{1/3}$ size effect ($R_i \equiv r_i \cdot A^{1/3}$) was considered in the calculations, but the asymmetry dependence on (N-Z)/A was ignored. Alternate radial dependence on mass and the asymmetry dependence are discussed below. The ESOM fitting followed the same procedures set forth above for the ISOM case. The primary impact of the ESOM approach is at the lower energies where the CN processes are changed relative to those of the ISOM. These changes lead to different parameter energy dependencies that extend to energies above 8 MeV. The calculations were tedious when dealing with the ESOM as the number of isotopes was increased six fold. The resulting ESOM parameters are given in Table 4.3.3. The energy dependencies of the real- and imaginary-potential strengths is shown in Fig. 4.3.1. The real strength falls with energy in the manner expected from a local-equivalent Hartree-Fock behavior, and imaginary strength increases with energy as more channels open. This ESOM provides an acceptable description of the elastic-scattering data base, as illustrated in Fig. 3.2.2. The total cross sections calculated with the ESOM are in reasonable agreement with the experimental values over the entire energy range 0 → 25+ MeV (see Fig. 4.1.1). The maximum difference between measured and calculated total cross sections is

Table 4.3.1. ISOM parameters deduced with the simple mono-isotopic assumptions of the text. Geometries are given in fermis, strengths, J_i, in volume-integrals-per-nucleon (MeV-fm^3) except for V_{so} (given in MeV), and energies, E, in MeV.

Real Potential

$J_v = 425 - 2.0 \cdot E$

$r_v^i = 1.2471$

$a_v = 0.6867$

Imaginary Potential

$J_w = 50.0 + 1.36 \cdot E$

$r_w^i = 1.35 - 0.0064 \cdot E$

a_w^{ii}, C = 0.58 fm, D = 5.48 MeV

Spin-Orbit Potential [WG86]

$V_{so} = 6.0075 - 0.015 \cdot E$

$r_{so}^i = 1.103$

$a_{so} = 0.56$ ·

---

[i] Where the radius $R_i = r_i \cdot A^{1/3}$.

[ii] a_w has the form $a_w = \dfrac{C \cdot (E - E_F)^2}{(E - E_F)^2 + D^2}$ where $E_F = -7.906$ MeV is the fermi energy, as discussed in the text.

Table 4.3.2. Strength function comparisons in units of 10^{-4}.

Isotope	Models				Expt.*
	A	B	C	D	
124					
s-wave	0.725	0.485 (0.355)	0.382	0.390	0.15±0.08
p-wave	4.191	3.584 (4.220)	3.142		3.5±0.3
122					
s-wave	0.652	0.406 (0.338)	0.351	0.380	0.3±0.12
p-wave	4.705	4.007 (4.440)	3.448		3.1±0.4
120					
s-wave	0.593	0.347 (0.325)	0.331	0.372	0.14±0.02
p-wave	5.270	4.475 (4.660)	3.789		2.10±0.20
118					
s-wave	0.548	0.305 (0.315)	0.322	0.365	0.46±0.21
p-wave	5.880	4.987 (4.870)	4.166		2.9±0.4
116					
s-wave	0.514	0.278 (0.308)	0.321	0.365	0.26±0.05
p-wave	6.516	5.538 (5.060)	4.580		3.8±0.3

A = ISOM potential of Table 4.3.1.
B = ESOM potential of Table 4.3.3. Parenthetical values are obtained using the isovector potential described in Section 4.6 of the text.
C = DOM potential of Table 4.4.1.
D = CCM potential of Table 4.5.1.
* Deduced from low-energy measurements as given in refs. [MDH81], [PS86] and [Nak+86].

≈ 3%, and it is generally much smaller. The ESOM strength functions differ from those of the ISOM (see Table 4.3.2), reflecting changes in the low-energy portion of the potential due to the detailed consideration of the isotopic structure.

Both the ISOM and ESOM confine the imaginary absorption potential to the nuclear surface. With increasing incident energy it is reasonable to expect the absorption to drift from the surface to the nuclear interior. There is a suggestion of such trend in the ESOM of Table 4.3.3 as at higher energies the diffuseness of the surface absorption broadens and its centroid moves toward smaller radii, even smaller than those of the real potential. It is common practice to roughly approximate this physical trend by the introduction of a volume-absorption potential whose magnitude increases with incident energy (see for example refs. [Rap+80], [BG69], [WG86] and [Gus+89]). The onset of volume absorption cited in the literature varies widely, from ≈ 10 MeV to above 30 MeV. A search was made for such a volume-absorption contribution. The geometries of the ESOM were assumed, and three-parameter elastic-scattering fits were carried out at energies above 10 MeV, varying the real, surface-imaginary and volume-imaginary potential strengths. Up to incident energies of ≈ 18 MeV no significant volume absorption could be identified. At 24 MeV the fitting of the data of ref. [Rap+80] suggested a small volume absorption of strength $J_{wvol} \approx 8.3$ MeV-fm^3. The uncertainty in this result was estimated to be perhaps 25 - 50%. The contribution had negligible effect on the definition of the overall elemental ESOM parameters of Table 4.3.3.

4.4. The Dispersive Optical Model (DOM)

The ESOM was extended to include the dispersion relationship linking real, V, and imaginary, W, potentials [Sat83]

$$V(r,E) = V_{HF} + \frac{P}{\pi} \int_{-\infty}^{+\infty} \frac{W(r,E')}{(E-E')}\, dE' \qquad (4.4.1)$$

where P denotes the principle value of the integral, V_{HF} is the local-equivalent Hartree-Fock potential, and E is energy. This relation results in a departure of V from V_{HF} at lower and bound energies, and leads to an energy dependence of the geometries of the simple ISOM or ESOM models. Eq. 4.4.1 can be reformulated in terms of volume-integrals-per-nucleon, J_i, resulting in

$$J_v(E) = J_{HF}(E) + \frac{P}{\pi} \int_{-\infty}^{+\infty} \frac{J_w(E')}{(E-E')}\, dE'. \qquad (4.4.2)$$

The integral can be broken in surface, ΔJ_s, and volume, ΔJ_{vo},

Table 4.3.3. ESOM parameters deduced with the elemental model of the text. Geometries are given in fermis, strengths, J_i, in volume-integrals-per-nucleon (MeV-fm^3) except for V_{so} (given in MeV), and energies, E, in MeV.

Real Potential

$J_v = 438.9 - 3.3956 \cdot E$

$r_v^i = 1.27 - 0.0028 \cdot E$

$a_v = 0.6888$

Imaginary Potential

$J_w = 53.99 + 0.94914 \cdot E$

$r_w^i = 1.38 - 0.0096 \cdot E$

a_w^{ii}, C = 0.7632 fm, D = 11.51 MeV

Spin-Orbit Potential [WG86]

$V_{so} = 6.0075 - 0.015 \cdot E$

$r_{so}^1 = 1.103$

$a_{so} = 0.56$

[i] Where the radius $R_i = r_i \cdot A^{1/3}$.

[ii] a_w has the form $a_w = \dfrac{C \cdot (E-E_F)^2}{(E-E_F)^2 + D^2}$ where $E_F = -7.906$ MeV is the fermi energy, as discussed in the text.

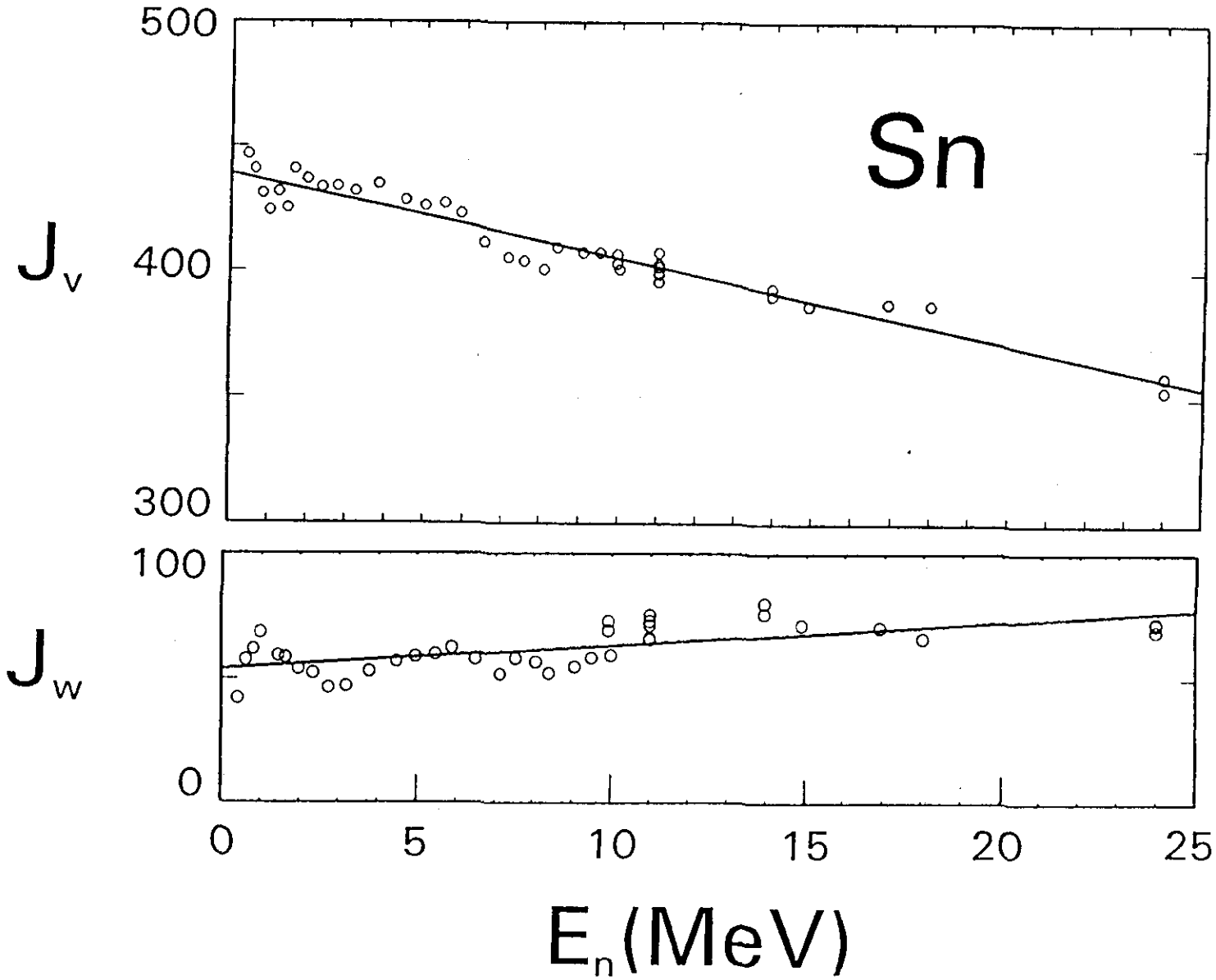

Fig. 4.3.1. Energy dependencies of the real, J_v, and imaginary, J_w, ESOM-potential strengths expressed as volume integrals per nucleon, J_i, in units of MeV-fm^3. Symbols indicate the results of fitting at individual energies and curves the parameterizations of Table 4.3.3.

components, where

$$\Delta J_S(E) = \frac{P}{\pi}\int_{-\infty}^{+\infty}\frac{J_S(E')}{(E-E')}\,dE', \qquad (4.4.3)$$

$$\Delta J_{VO}(E) = \frac{P}{\pi}\int_{-\infty}^{+\infty}\frac{J_{VO}(E')}{(E-E')}\,dE' \qquad (4.4.4)$$

and J_S and J_{VO} are volume-integrals-per-nucleon of the surface and volume absorption, respectively. Thus

$$J_V(E) = J_{HF}(E) + \Delta J_{VO}(E) + \Delta J_S(E) \qquad (4.4.5)$$

or $$J_V(E) = J_{eff}(E) + \Delta J_S(E) \qquad (4.4.6)$$

where $J_{eff}(E) \equiv J_{HF}(E) + \Delta J_{VO}(E)$. The above ESOM interpretation indicates that J_{VO} is very small at 24 MeV and negligible at lower energies. Furthermore, both $J_{HF}(E)$ and $\Delta J_{VO}(E)$ are approximately linear functions of energy over the range -30 to +30 MeV and thus the two components of $J_{eff}(E)$ can not be experimentally identified. In view of this, and the very small magnitude of $J_{VO}(E)$ at even 24 MeV, no effort was made to evaluate $\Delta J_{VO}(E)$. For convenience, the ratio

$$\lambda(E) \equiv \Delta J_S(E)/J_S(E) \qquad (4.4.7)$$

was defined. $\lambda(E)$ is clearly the quantity by which the surface-imaginary strength, $J_S(E)$, is multiplied to obtain the surface-peaked component of the real potential, $\Delta J_S(E)$, resulting from the integral of Eq. 4.4.1. $\lambda(E)$ was evaluated from the parameters of the ESOM (Table 4.3.3) using the following simple assumptions:- i) J_S is symmetric about the fermi surface E_F (using ^{118}Sn, E_F = -7.906 MeV). ii) For energies $2\cdot E_F < E < 0$ $J_S(E)$ was assumed to have the parabolic form $J_S = (J_O/E_F^2)\cdot(E-E_F)^2$ with $J_O \equiv J_S$ at the E = 0 value of the ESOM. iii) For 0 < E < 20 MeV $J_S(E)$ was taken from the ESOM of Table 4.3.3. iv) Above 20 MeV $J_S(E)$ was assumed to decrease linearly with E to a zero value at 60 MeV. The latter end point is consistent with the range of values quoted in ref. [Gus+89], and reasonable alternate choices of end point had a minor influence on the results. Assumption iv) suggests that the volume absorption increases from very small values at ≈ 20 MeV to a constant value of $J_{VO}(E) \approx 80$ MeV-fm^3 at 60 MeV. The energy dependencies of $\Delta J_S(E)$ and $\lambda(E)$, calculated with

the above assumptions, are shown in Figs. 4.4.1 and 4.4.2. From Fig. 4.4.2 it is clear that the effect of the dispersion integral of Eq. 4.4.1 is to add a surface component to the Saxon-Woods Hartree-Fock potential at lower energies, decreasing with energy to zero at ≈ 16 MeV, and then subtracting a surface component at higher energies. The surface component is quite significant at the extremes of the energy range (i.e., at 0 and 25 MeV). The above simple approach to the DOM has been successfully used by the author and his co-workers on a number of occasions [Smi+92].

Using the above $\lambda(E)$ values, the entire fitting procedure employed for the ESOM was repeated. The resulting DOM parameters are given in Table 4.4.1. The energy dependencies of the real- and imaginary-potential strengths are shown in Fig. 4.4.3. The DOM also gave an acceptable description of the elastic-scattering data base as shown in Fig. 4.4.4. The quality of the description is equivalent to that obtained with the ESOM. There was a similar good agreement between measured total cross sections and those calculated with the DOM (see Fig. 4.1.1), with the DOM result preferable at the very low energies. The strength functions calculated with the DOM (Table 4.3.2) are significantly different from those obtained with the ISOM or ESOM reflecting the relatively large contribution of the dispersion integral at low energies.

4.5. The Coupled-Channels Model (CCM)

It is evident from the inelastic-scattering results (see Figs. 3.3.1 and 3.3.2) that there is a significant direct neutron interaction with the tin isotopes in the energy range of the present considerations. The even tin isotopes display characteristics of collective vibrators with a yrast (2^+ one-phonon) level at an excitation of approximately 1.1 MeV. However, they are not simple vibrators as the quadrupole moments are not zero and the two-phonon levels are not well defined. Most of the even isotopes have an octupole 3^- vibrational level at ≈ 2.5 MeV. β_2 values deduced from coulomb-excitation studies are relatively small (≈ 0.10) [Ram+87]. A coupled-channels model interpretation in the scope of the ESOM, above, dealing with the five prominent even isotopes, one- and two-phonon vibrations and the octupole excitations is prohibitively time consuming. Therefore, in the coupled-channels model derivation some simplifying assumptions were made:- i) Elemental tin was assumed to consist of a single isotope having the elemental mass of 118.7 and the excited structure of the ^{118}Sn. This is the same assumption as that made for the ISOM discussed above. ii) The interaction was taken to be a simple one-phonon vibrational process, coupling ground (0^+) and yrast (2^+) states. iii) β_2 was taken to be 0.1081, the weighted average of the major even isotopic values deduced from coulomb-excitation considerations [Ram+87]. iv) The

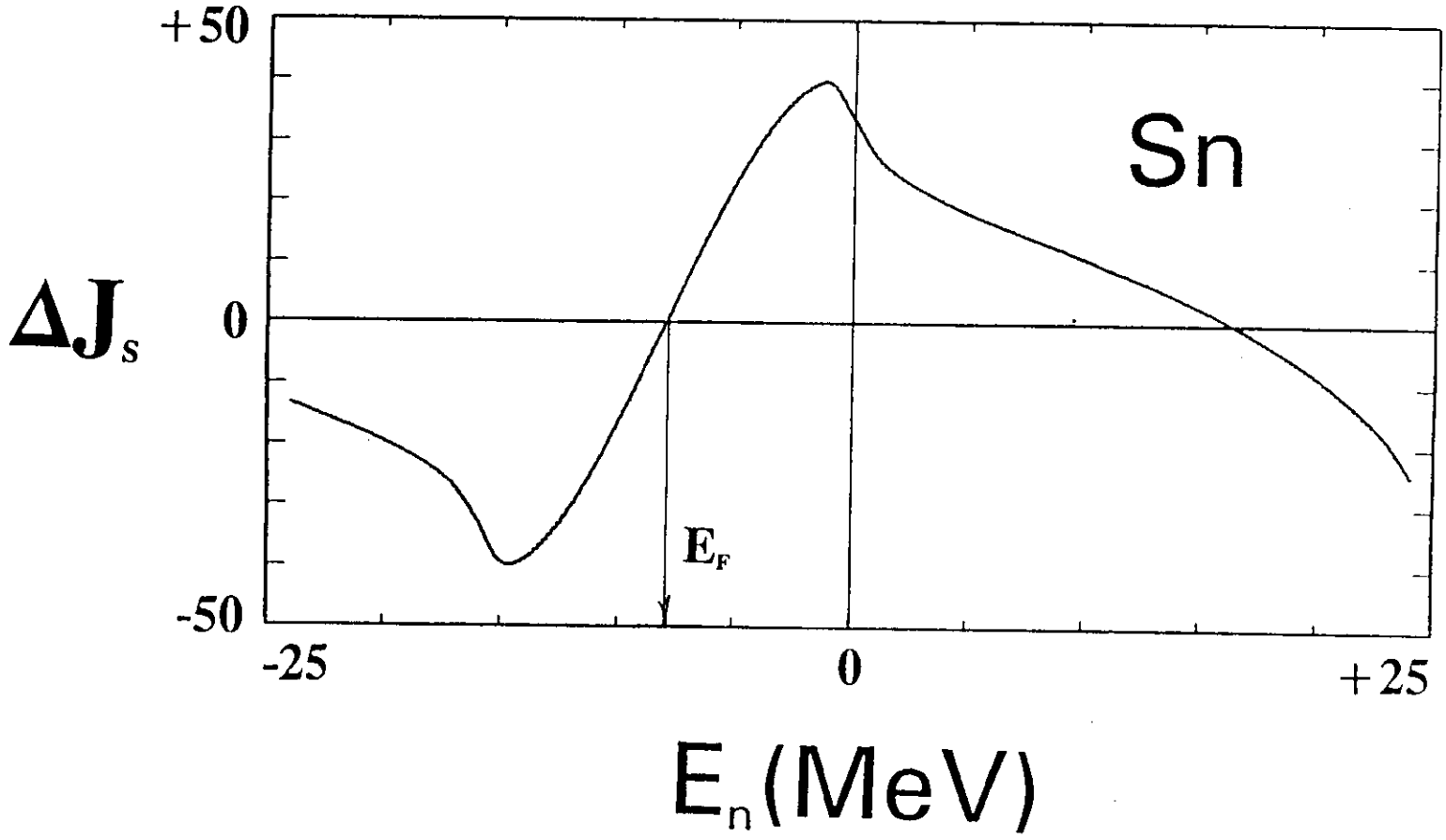

Fig. 4.4.1. The energy dependence of $\Delta J_s(E)$ of Eq. 4.4.3. ΔJ_s is in units of MeV-fm^3.

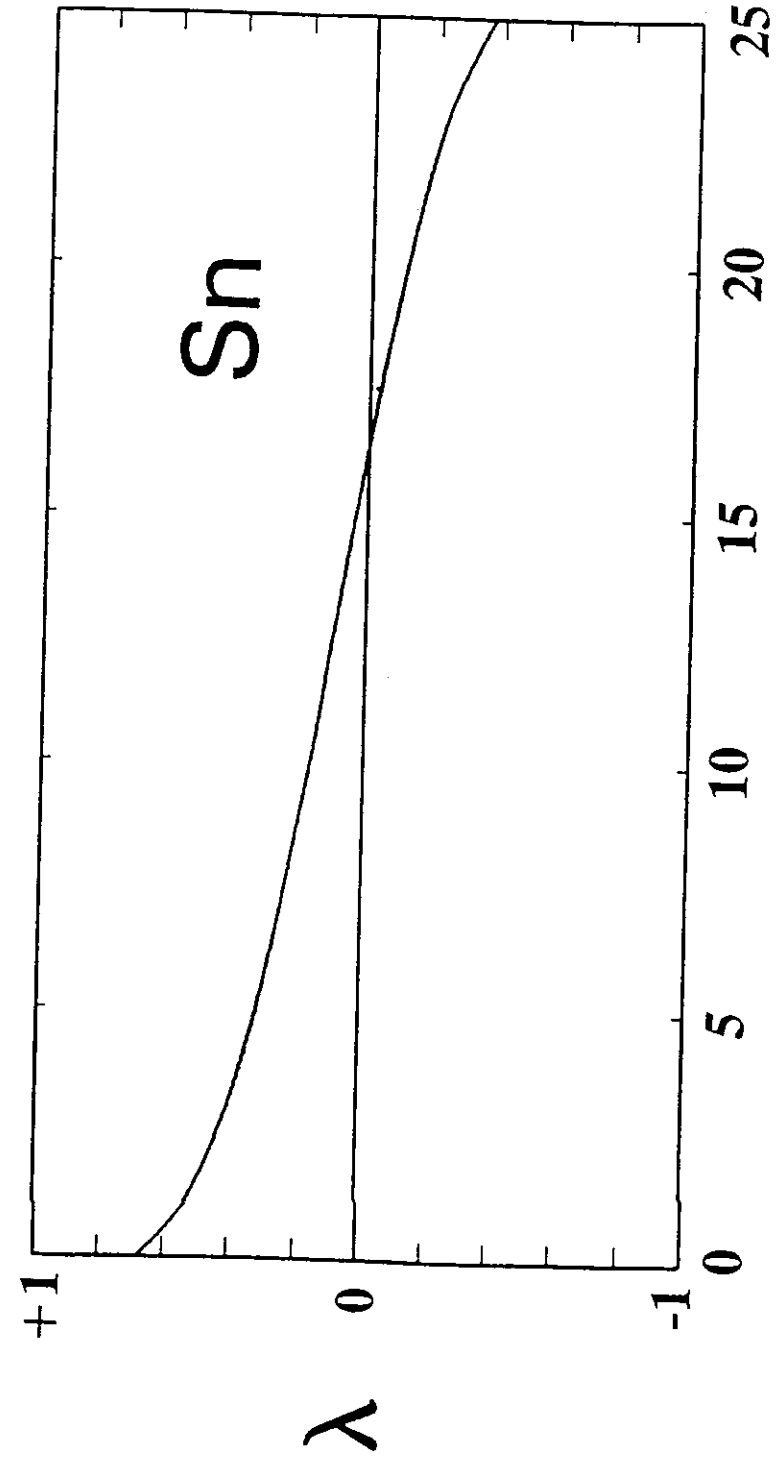

Fig. 4.4.2. The energy dependence of the ratio $\lambda(E)$ of Eq. 4.4.7.

Table 4.4.1. DOM parameters derived as discussed in the text. Geometries are given in fermis, strengths, J_i, in volume-integrals-per-nculeon (MeV-fm^3) except for V_{so} (given in MeV), and energies, E, in MeV.

Real Potential

$J_v = 412.1 - 1.1228 \cdot E$

$r_v^i = 1.2471$

$a_v = 0.6809$

Imaginary Potential

$J_w = 57.85 + 0.8087 \cdot E$

$r_w^i = 1.37 - 0.0104 \cdot E \quad (E<10 \text{ MeV})$

$= 1.28 - 0.0014 \cdot E \quad (E>10 \text{ MeV})$

$a_w = 0.260 + 0.0312 \cdot E \quad (E<8.5 \text{ MeV})$

$= 0.5250 \quad (E>8.5)$

Spin-Orbit Potential [WG86]

$V_{so} = 6.0075 - 0.015 \cdot E$

$r_{so}^i = 1.103$

$a_{so} = 0.56$

[i] Where the radius $R_i = r_i \cdot A^{1/3}$.

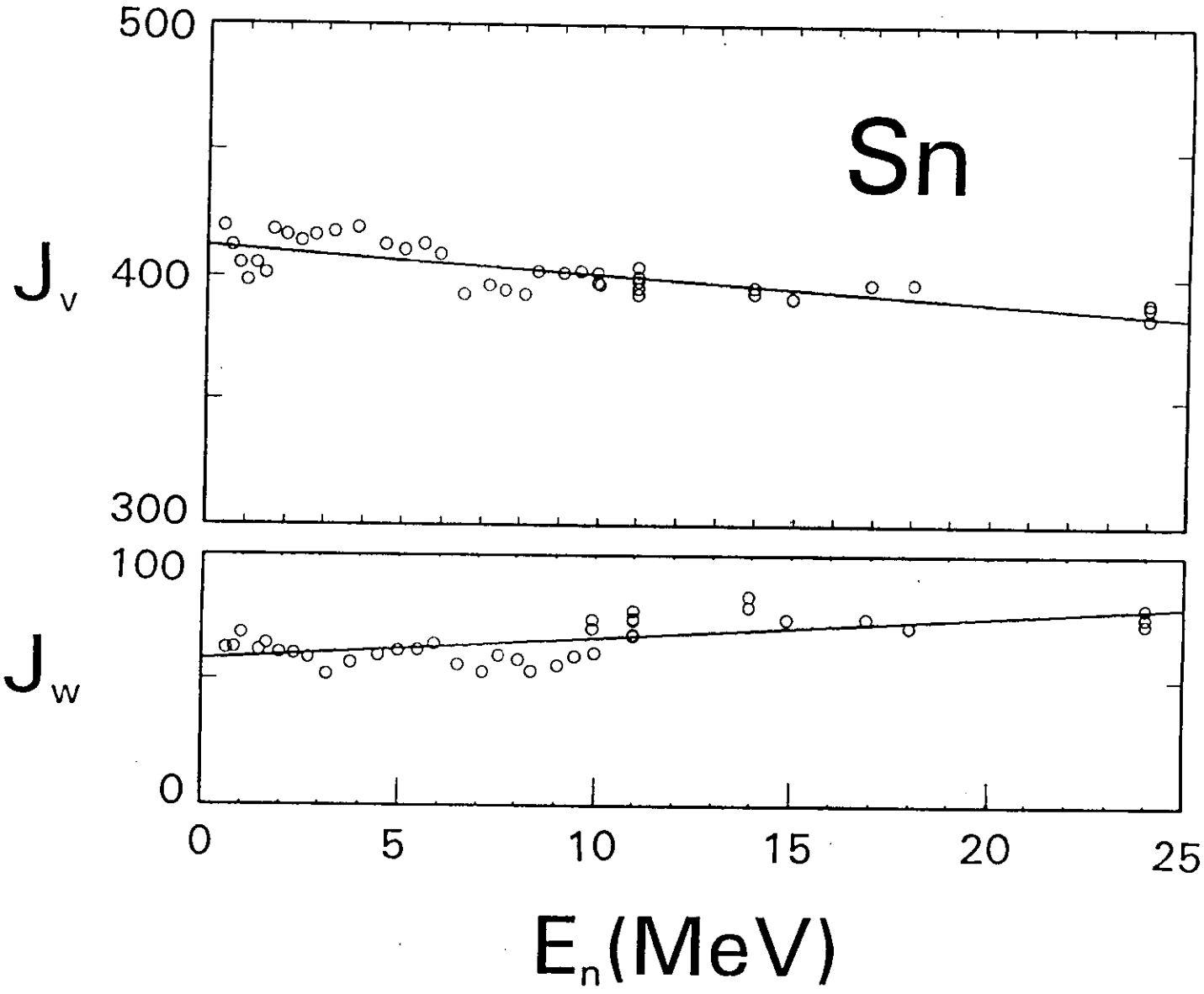

Fig. 4.4.3. The energy dependencies of the real, J_v, and imaginary, J_w, strengths of the DOM. The nomenclature is the same as for Fig. 4.3.1.

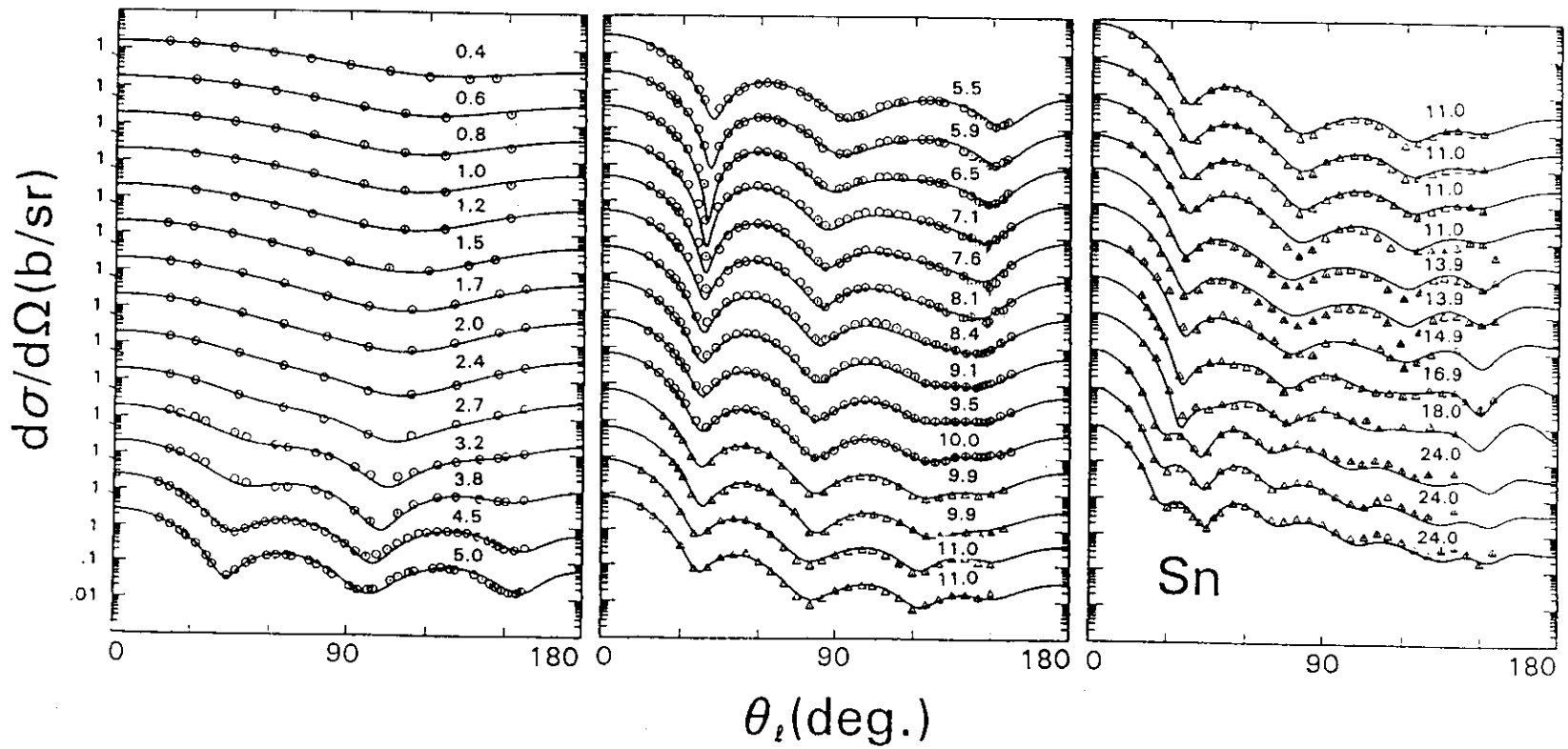

Fig. 4.4.4. Comparison of the tin elastic-scattering data base (symbols) with the results of DOM calculations (curves). The nomenclature is identical to that of Fig. 3.2.2.

elastic-scattering data base was corrected for compound-elastic contributions using the ESOM model. These corrections were applicable only below 8 MeV, but were very large at low energies. The latter fact resulted in large uncertainties and thus the CCM derivation was limited to incident energies of $\geq$ 1.5 MeV. The correction procedure, of course, employed spherical transmission coefficients but, in view of the small β_2 values, this should result in minor perturbations. The "corrected" elastic-scattering data base is shown in Fig. 4.5.1.

With the above assumptions, coupled-channel fitting was carried out following the steps described above for the spherical models. The calculations employed the coupled-channels computer code ANLECIS [Mol81]. The resulting potential parameters are given in Table 4.5.1. The energy dependencies of the potential strengths behave in a reasonable manner as illustrated in Fig. 4.5.2. The calculated elastic-scattering distributions are consistent with the data base from which they were derived as shown in Fig. 4.5.1. It is noted that the agreement between measured and calculated values in the range $\approx 6 \rightarrow 7$ MeV is better than obtained with either the ESOM or DOM where the latter two potentials result in too-low cross sections at the first minimum of the elastic distributions. The measured total cross sections are reasonably described, as shown in Fig. 4.1.1. The strength functions implied by the CCM are given in Table 4.3.2. The cross sections for the inelastic excitation of the yrast (2^+) level calculated with the CCM are in good agreement with the measured values as shown in Fig. 3.3.2.

4.6. Isoscaler and Isovector the Potentials

It is well known that the optical-model potential is generally dependent on the nuclear asymmetry $(N-Z)/A \equiv \eta$ [Lan62]. This dependence is usually expressed in the real(V) and imaginary(W) potential forms

$$V = V_0 \pm V_1 \cdot \eta \qquad (4.6.1)$$
$$W = W_0 \pm W_1 \cdot \eta,$$

where "+" refers to protons and "-" to neutrons [Sat69]. Eqs. 4.6.1 are not sufficient specification as the potential strengths are dependent upon geometry (i.e., the well known VR^n and Wa ambiguities). Failure to recognize this fact may have contributed to the spread in V_1 and W_1 value found in the literature. To avoid this problem, the present asymmetry considerations are formulated in terms of volume-integrals-per-nucleon. In that form, Eqs. 4.6.1 become

$$J_v = J_{ov} - J_{v1} \cdot \eta \qquad (4.6.2)$$
$$J_w = J_{ow} - J_{w1} \cdot \eta,$$

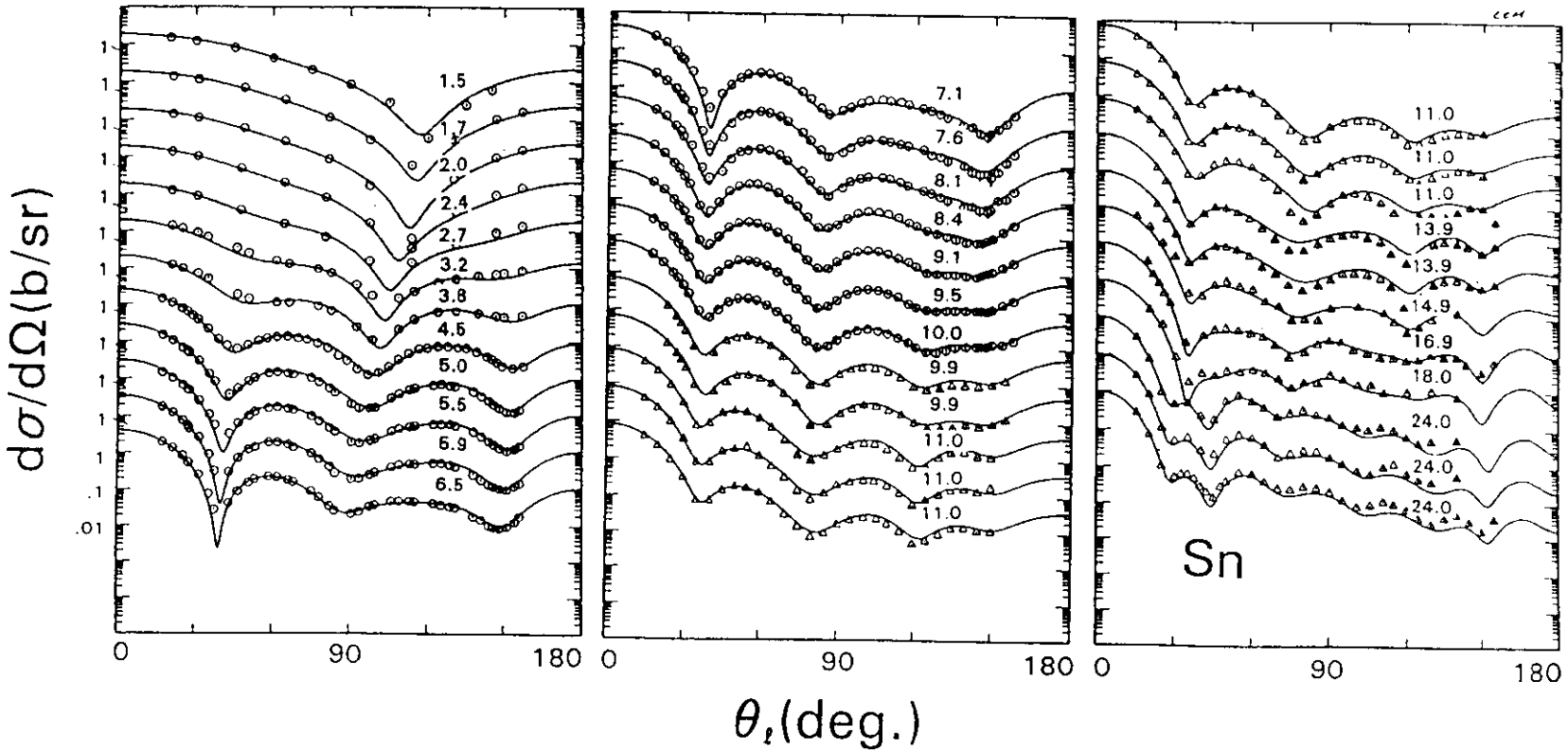

Fig. 4.5.1. Elastic-scattering cross sections of tin. Symbols indicate the experimental values where "0" are elemental and "Δ" isotopic. The experimental results have been corrected for CE contributions below 8 MeV. Curves indicate the results obtained from the CCM calculations. Approximate incident energies are numerically indicated in MeV.

Table 4.5.1. CCM parameters deduced as described in the text. Geometries are given in fermis, strengths, J_i, in volume-integrals-per-nucleon (MeV-fm^3) except for V_{so} (given in MeV), and energies, E, in MeV.

Real Potential

$J_v = 436.7 - 3.8326 \cdot E$

$r_v^i = 1.2762 - 0.00493 \cdot E$

$a_v = 0.7044$

Imaginary Potential

$J_w = 39.95 + 1.4634 \cdot E$

$r_w^i = 1.3941 - 0.00985 \cdot E$

a_w^{ii}, C = 0.80 fm, D = 10.77 MeV

Spin-Orbit Potential [WG86]

$V_{so} = 6.0075 - 0.015 \cdot E$

$r_{so}^i = 1.103$

$a_{so} = 0.56$

Deformation $\beta_2 = 0.1081$

[i] Where the radius $R_i = r_i \cdot A^{1/3}$.

[ii] a_w has the form $a_w = \frac{C \cdot (E-E_F)^2}{(E-E_F)^2 + D^2}$ where $E_F = -7.906$ MeV is the fermi energy, as discussed in the text.

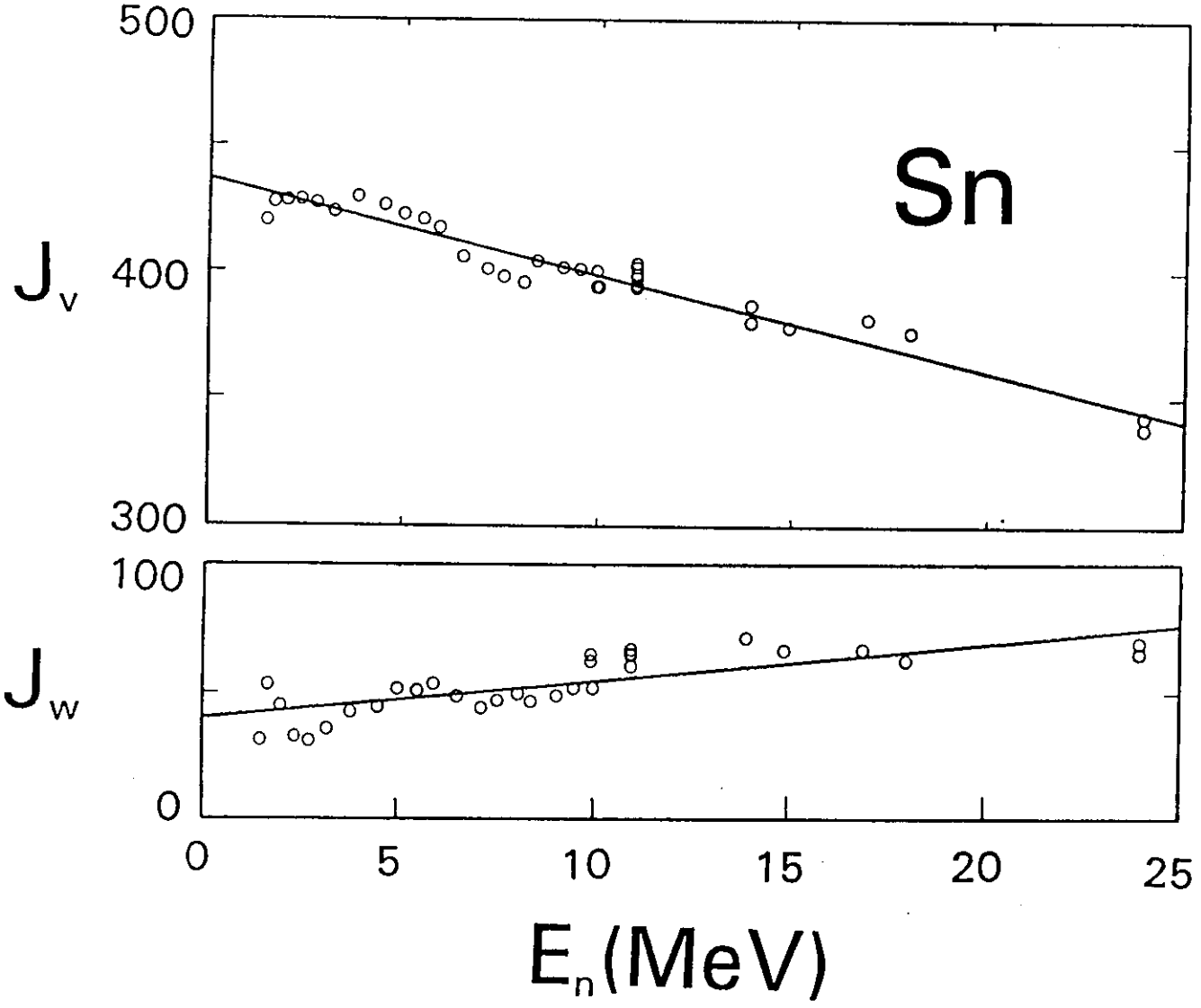

Fig. 4.5.2. Energy dependencies of real, J_v, and imaginary, J_w, CCM potential strengths. Symbols indicate the results of fitting individual distributions, and the curves the parameterization of Table 4.5.1. Strengths are given as volume-integrals-per-nucleon in MeV-fm^3.

or

$$J_v = J_{ov}\,(1 - \xi_v \cdot \eta) \qquad (4.6.3)$$
$$J_w = J_{ow}\,(1 - \xi_w \cdot \eta)$$

for neutrons, where $\xi_i = J_{i1}/J_{oi}$. The present considerations, in the form of Eqs. 4.6.3, are essentially geometry independent over limited mass ranges.

All of the above elastic-scattering data base is isotopic above 10 MeV. The most comprehensive set of elastic-scattering measurements consists of the five even tin isotopes $^{116\to124}$Sn at 11 MeV reported by Rapaport et al. [Rap+80]. This data set appears of high quality and has good angular coverage. The real- and imaginary-potential strengths were determined by fitting each of these distributions assuming the potential geometries of the above ESOM, DOM and CCM models. The resulting J_v values were a linear function of η, as illustrated in Fig. 4.6.1, with the numerical values $J_v = 432\cdot(1-0.45\cdot\eta)$, $= 430\cdot(1-0.44\cdot\eta)$ and $= 428\cdot(1-0.45\cdot\eta)$ using the ESOM, DOM and CCM potentials, respectively. The corresponding J_w values were $J_w = 103.5\cdot(1-1.81\cdot\eta)$, $= 100.6\cdot(1-1.84\cdot\eta)$ and $= 89.6\cdot(1-1.73\cdot\eta)$. Inherent in these results is the assumption that the isoscaler and isovector potentials have the same SW form and that $R_i \equiv r_i A^{1/3}$. *Other formulations of* R_i *have been proposed as the* result of electron, proton and neutron studies ([Rap+80] [Har+84]), and the effect of some of these alternatives was examined in ref. [Rap+80]. In the present work, two alternatives were investigated. The most acute assumption set R_i = constant = the elemental radius (i.e., $R_i = r_i \cdot 118.7^{1/3}$). The consequence was to increase ξ_v by ≈ 50% and ξ_w by ≈ 20%. Concurrently, chi-square resulting from the fitting procedures significantly increased. A more realistic alternative is $R_i = r_i \cdot A^{1/3}$, where $r_i = r_{io} + 0.4/A^{1/3}$. r_{io} was determined from the elemental ESOM and DOM potentials. Radial behavior of this nature has been suggested for both neutron and proton potentials ([Chi+90], [Mey73]). The resulting J_{oi} and ξ_i values were essentially the same as those obtained with the simple $R = r\cdot A^{1/3}$ relationship. Rapaport et al. *[Rap+80] also concluded that* $R_i = r_i \cdot A^{1/3}$ *gives a good* representation.

The data base contains 24 MeV elastic-scattering distributions for ^{116,118} and ^{124}Sn from ref. [Rap+80]. The mass range is limited, and the quality and the angular coverage of these distributions does

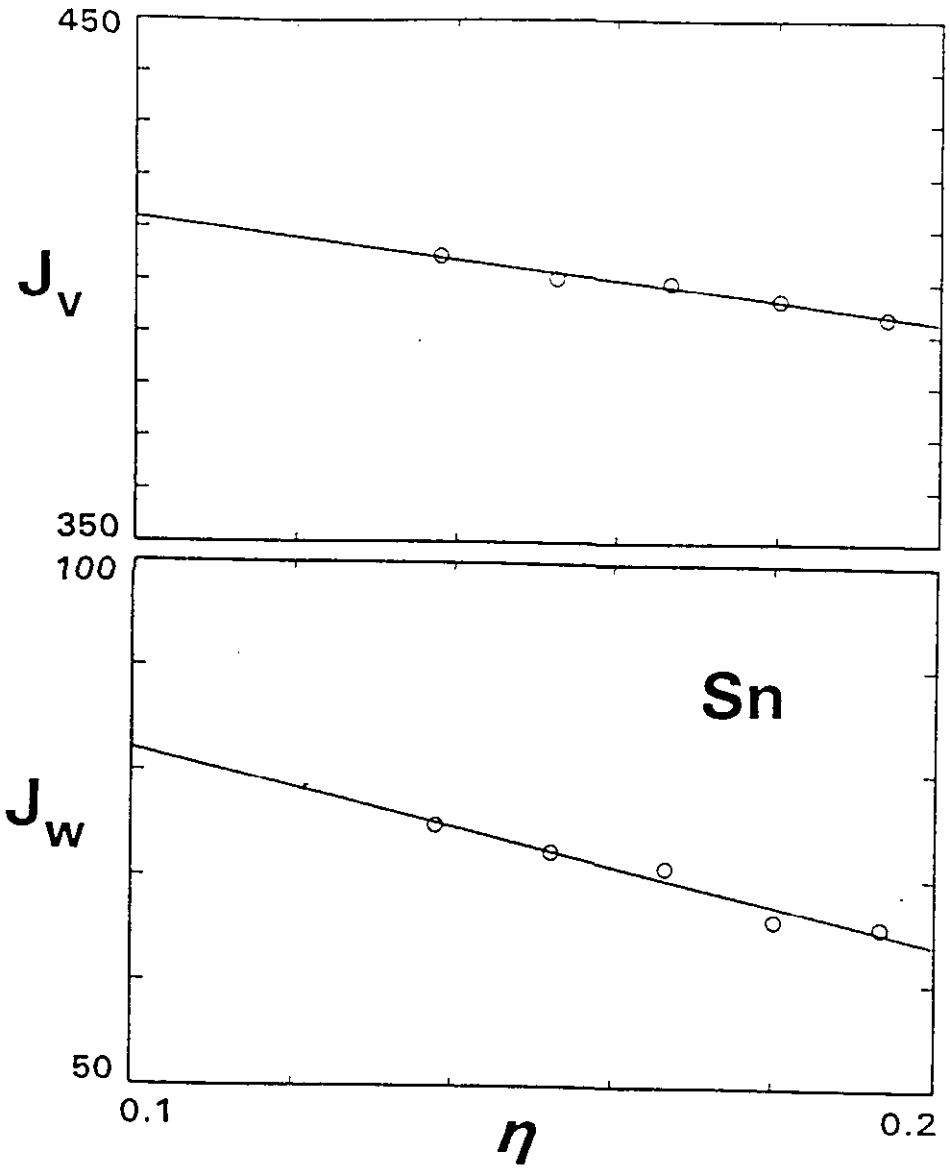

Fig. 4.6.1. Asymmetry, $\eta \equiv (N-Z)/A$, dependence of real, J_v, and imaginary, J_w, potential strengths of the tin isotopes at 11 MeV. The symbols indicate the ESOM results described in the text and curves the least-square fits to the model values. Strengths are given as volume-integrals-per-nucleon with the *dimensionality* of MeV-fm^3.

not appear as good as the 11 MeV data from the same group. Using the same fitting procedures, the ξ_v deduced from the 24 MeV data was 0.256 and 0.299, using DOM and ESOM geometries, respectively. The J_w values resulting from fitting the 24 MeV data had considerable scatter, but ξ_w tends to be ≈ 50% of that found at 11 MeV. Ref. [Gus+89] reports 116 and 120Sn elastic-scattering distributions at ≈ 10 and 14 MeV. There are only two nearby mass values and there is a tendency for these data sets to yield model parameters somewhat different from the body of the data base. With these caveats, the isotopic fitting was extended to 10 and 14 MeV using the ESOM geometries. At 10 MeV $J_v = 439\cdot(1-0.51\cdot\eta)$ and $J_w = 102.2\cdot(1-1.93\cdot\eta)$. These values are similar to the equivalent quantities at 11 MeV. However, at 14 MeV $J_v = 414\cdot(1-0.29\cdot\eta)$ and $J_w = 104.8\cdot(1-1.48\cdot\eta)$. The ξ_i of these 14-MeV results are sharply smaller than obtained at 10 or 11 MeV, and more like the 24 MeV results.

There are several additional and isolated isotopic distributions in the data base. They were not used in the asymmetry considerations as the results would be sensitive to small systematic discrepancies between measured data sets from different sources.

5. Discussion and Summary

5.1. Potential Comparisons

In Section 4, four models were deduced from the data base, the ISOM, ESOM, DOM and CCM. In this discussion attention will be confined to the latter three as the ISOM is clearly a first approximation that does not properly treat CN processes at lower energies, and probably as a consequence has somewhat different parameters.

The ESOM, DOM and CCM a_v values are constant with energy and have an average value of 0.6914 fm. The average deviation from the mean is 1.15%. The energy independence is consistent with the global nature of a_v noted in many studies at this laboratory [Smi+92], and the magnitudes are similar to those obtained in other studies at this laboratory and to values reported in the literature (see illustrative examples of Table 5.1.1). The present models were deduced quite independently over many months, and it is remarkable that the resulting a_v values are so similar, particularly as they result from the initial six-parameter fitting.

The real radius, r_v, is difficult to determine due to the strong correlation between real-potential radius and strength. Despite this, the behavior of the three models is physically reasonable. The r_v of the CCM and ESOM decrease with energy from essentially the same value

Table 5.1.1. Some illustrative comparisons of geometric model parameters where r_v and a_v are the reduced radius and diffuseness of the real potential, and r_w and a_w the respective values for the surface-imaginary potential. (Some of the citations from the literature contain volume absorption at higher energies). The comparisons are made at 11 MeV and for the elemental mass A=118.7. All values are in fermis.

Ref.	r_v	a_v	r_w	a_w
Present work				
ESOM	1.2392	0.6888	1.2744	0.5568
DOM	1.2471	0.6809	1.2556	0.5250
CCM	1.2220	0.7044	1.2858	0.6040
[BG69]	1.170	0.750	1.260	0.580
[Rap+80] "ave." values of ref.	1.200	0.686	1.300	0.632
[Fer+77] Table 3 of ref.	1.226	0.605	1.140	0.733
[Gus+89]	1.230	0.660	1.250	0.540
[WG86]	1.219	0.688	1.282	0.512
[Rap+79]	1.198	0.663	1.295	0.590
[WH64]	1.2812	0.660	1.2439	0.480
[Pat+76]	1.170	0.750	1.320	0.6203

at zero energy, the former somewhat more rapidly. The energy dependence is sensitive to the higher-energy aspects of the data base which displays some inconsistency. In contrast, the DOM r_v is constant with energy. In the DOM case the surface component of the real potential has been explicitly dealt with. Without this one expects a trend toward an energy dependence of r_v of the type displayed by the ESOM and CCM as a surface component is added to the SW form at lower energies and subtracted at higher energies. The CCM and ESOM r_v values appear to be consistent with systematics at 8 MeV. It is shown in ref. [Chi+90] that at 8 MeV $r_v = 1.154 + 0.4074/A^{1/3}$ fm, or for elemental tin $r_v = 1.2369$ fm. A qualitatively similar mass dependence of the rms real-potential radius was suggested long ago [HW68]. The mean of the CCM and ESOM values at 8 MeV is 1.2420 fm (and the DOM value is 1.2471), differing from the systemic value by only ≈ 0.4%. Thus the present results are consistent with systematic trends in r_v which indicate a decreasing r_v with mass ([Mey73] [Chi+92]), and suggest that r_v will be energy dependent if the dispersion effect is ignored. Clearly the energy-dependent trends of the present parameterizations can not extend to unlimited energies, and r_v must approach some asymptotic value at the upper limit of the energy range of the present interpretations. The present ESOM and CCM results are qualitatively consistent with values found in the literature (as illustrated in Table 5.1.1) but comparisons are complicated by the energy independence of most previously reported r_v values.

The CCM and ESOM real-potential strengths are quit similar, differing by 0.5% at zero energy and by 3.7% at 25 MeV. The difference in the energy dependence may reflect small physical effects but it is also sensitive to the high-energy distributions of the data base. The real potential of the DOM is different, as it should be since it does not include the ΔJ_s of Fig. 4.4.1. When that is added the DOM J_v is similar to those of the CCM and ESOM. Systematics predict $J_v = 406.33$ MeV-fm^3 for the elemental mass at 8 MeV [Chi+90]. The comparable average of ESOM and CCM values is 408.9 MeV-fm^3, a difference of only 0.6%. "Local" (to the tin region) and "global" models reported in the literature scatter about the present potentials in strength and energy dependence, as illustrated in Table 5.1.2. There have been a number of considerations of the equation of state, largely based upon proton data. An example is the work of Bauer et al. [Bau+82]. For neutrons incident on elemental tin those authors give $J_v = 428.01 - 3.2572 \cdot E + 0.0062 \cdot E^2$. The latter expression is well represented by $J_v = 427.6 - 3.103 \cdot E$ up to ≈ 30 MeV, and is very close to the present ESOM and CCM results. In both the ESOM and CCM,

the energy dependence of J_v may be slightly too large due to the neglect of the dispersion integral while it may be somewhat too small in the case of the DOM due to the simple approximations used in the calculations.

The imaginary potential is sensitive to structure effects and tin is magic in proton number. Thus the imaginary potential of tin may not be of a general nature. The r_w of the ESOM and CCM are very similar with relatively large values at zero energy that decrease with energy to approach (or even fall somewhat below) r_v at 25 MeV. Large r_w values have long been suggested by studies of low-energy neutron interactions [Mol63]. The r_w values found in the literature scatter, as illustrated in Table 5.1.1. The imaginary diffuseness is difficult to determine due to the strong correlation with the imaginary strength. However, the a_w values obtained with the ESOM and CCM are relatively consistent and both indicate small values at low energies, rising to approach a constant value of ≈ 0.78 fm at 25 MeV. The parameterization implies that $a_w \rightarrow 0$ at E_F. Such a behavior has long been observed at this laboratory [Smi+92]. Both ESOM and CCM J_w values increase with energy as one would expect from the opening of additional channels. The zero-energy magnitudes are different, with the CCM value being smaller as more channels have been explicitly treated in the model. As noted above, a volume absorption was identified at ≈ 24 MeV but it is so small that it had very little effect on the model interpretations. Similar small volume-absorption strengths have been noted at ≈ 25 MeV and above ([Rap+80], [Bee+70]). It is often assumed that the volume contribution extends to lower energies, however there appears to be no experimental support for such a behavior. The character of the DOM imaginary potential is somewhat different from that of the ESOM and CCM. It was obtained quite independently and the a_w parameterization is formally different but leads to qualitatively the same results. The r_w is large at zero energy and decreases with energy. The a_w is small at zero energy and rises to a constant value, and the strength increases with energy.

5.2. Total Cross Sections

Above ≈ 0.8 MeV all of the present potentials give essentially the same total-cross-section results, all of which are reasonably consistent with the measured values to well above 25 MeV, as illustrated in Fig. 4.1.1. The maximum difference between measured and calculated values is only $\lesssim 3\%$ at about 12 MeV. Such a difference is of the same order as the experimental uncertainties, though it appears systematic. At lower energies the calculated results differ by few percent, but these differences are barely outside the experimental uncertainties. The DOM results appear a bit more consistent with the measured values which is not surprising as

Table 5.1.2. Illustrative comparative potential energy dependencies where J_V refers to the real potential and J_W the surface-imaginary potential. J-values are given in volume-integrals-per nucleon in dimensions of Mev-fm^3, energy, E, is in MeV, and normalization is to the elemental mass A = 118.7 including isovector corrections. "*" notes J_W values where significant volume absorption is present at higher energies.

Present work		
ESOM	J_V=438.9-3.40·E	J_W=54.0+0.95·E
DOM	J_V=412.1-1.12·E	J_W=57.9+0.81·E
CCM	J_V=436.7-3.83·E	J_W=40.0+1.46·E
[Bau+82]	J_V=427.6-3.10·E	------
Linear equivalent		
[WG86]	J_V=428.4-2.55·E	J_W^*=74.8-1.38·E
[BG69]	J_V=411.5-2.51·E	J_W^*=107.6-2.4·E
[Gus+89]	J_V=424.2-1.92·E	J_W=6.86+15.1·$\sqrt{E}$, E<13
[JLM76]	$J_V \approx$ 500 - 2.8·E	------
Theory		
[WH64]	J_V=459.1-2.61·E+ 0.018·E^2	J_W=73.8-0.41·E
[Rap+79]	J_V=410.2-2.43·E	J_W=23.6+4.16·E, E≤15
[Pat+76]	J_V=415.4-2.51·E	J_W^*=27.8+4.6·E

the effect of the dispersion relationship is felt at low energies. There have been a few scattered isotopic total cross sections reported in the literature [Rap+80]. The present potentials, including the present isovector contributions, are consistent with those results. However, the reported isotopic total cross sections are not highly accurate nor energy comprehensive and thus do not provide a particularly stringent test of the models.

5.3. Strength Functions

Strength functions deduced from resonance measurements are frequently used to assess the low-energy behavior of model interpretations such as those of the present work. The approach is of questionable merit in the present context as:- i) isotopic tin strength functions are not very well known (e.g., they vary by factors of two, do not follow systematic mass dependent trends, and in many cases are quite uncertain), ii) the tin isotopes are in the minimum of the s-wave strength function distribution with mass, and iii) it has been argued [Sha63] that the S_0 strength functions of the tin isotopes are strongly influenced by doorway-state configurations that are not consistent with the concepts of optical and coupled-channels models. Despite these caveats, the ESOM, DOM and CCM provide results that are qualitatively consistent with experimentally-deduced strength functions, as summarized in Table 4.3.2. The S_0 values obtained with the ESOM, particularly when adjusted to include isospin effects, are similar to the experimentally-deduced results, given the scatter of the latter. The S_1 comparisons are of a similar qualitative character. The comparisons are arguably improved when the DOM or CCM are used. Most "global" SOM's give considerably larger S_0 values in this mass region. SOM's specifically tailored to low energies and the strength functions, such as that of ref. [Mol63], give better results, but they are far less suitable in the MeV region. Some reported studies ([NDC72] [Gus+89]) suggest a sharp decrease in the imaginary potential strength at low energies (e.g., following $\sqrt{E}$) in order to obtain low strength-function values. Such a behavior is not consistent with theoretical concepts which suggest the J_w goes to zero at the fermi energy ([BR78], [JLM76]), and is in contrast to the present models where the availability of extensive low-energy data leads to increasing imaginary diffuseness with energy in a quite natural manner while at the same time following the overall trends in the imaginary strength, and in a way consistent with behavior in other mass regions [Smi+92]. The dichotomy between low- and high-energy SOM's has long been evident, and suggests that the potentials are energy dependent in strengths and/or geometries. The latter are characteristic of the present interpretations and, perhaps for that reason, a physically reasonable unification of low- and high-energy representations is achieved.

5.4. Polarization

The calculation of scattered-neutron polarizations is primarily governed by the spin-orbit potential. The present work provides no new experimental polarization information. However, it is of interest to compare the scattered-neutron polarizations calculated with the present models with the reported experimental values. The 10 and 14 MeV polarizations of elastically-scattered neutrons were calculated with the present ESOM and CCM. These were compared with the measured and calculated results of refs. [Del+83] and [Gus+89]. Although no effort was made to adjust the ESOM or CCM potentials to optimize the descriptions of the measured polarizations, the comparisons were encouraging. For example, Fig. 5.4.1 compares the measured polarization results for elastic scattering of 10 MeV neutrons from ^{120}Sn with those calculated with the ESOM and CCM models. The descriptions approach the quality of interpretations specifically directed toward polarizations (as illustrated in Fig. 6 of ref. [Gus+89]) with no adjustments of the present models. This is perhaps not too surprising as the "global" spin-orbit parameters of ref. [WG86] used in the present work probably gave considerable emphasis to polarization phenomena.

5.5. Inelastic Scattering and Deformation

Simplifying assumptions were made in Section 4 in the calculation of inelastic-scattering cross sections comparable with the present element measurements. It was assumed that the element was reasonably represented by:- i) an even isotope with the elemental mass of 118.7, ii) with a yrast (2^+) level at 1.15 MeV, iii) 0^+, 2^+ and 4^+ levels at 2.1, 2,2 and 2.3 MeV, respectively, and iv) a 3^- level at 2.27 MeV. The first level was assumed to be a one-phonon vibrational state, followed by the two-phonon triplet and then the octupole vibrational level. β_2 was taken to be 0.1081 (the elemental average of the β_2^{EM} values of the prominent even isotopes [Ram+87]), and β_3 taken to be 0.160 ([Gus+89], [Mak+68]). The assumptions obviously ignore the small perturbations from the odd isotopes and variations of β_i with isotope. The calculations used the CCM with the parameters of Table 4.5.1. These are reasonable approximations in the context of the complexity of the elemental experimental values and the results were encouraging, as illustrated by the comparisons of measured and calculated angle-integrated cross sections shown in Fig. 3.3.2. The calculated excitations of the observed 1.15 MeV level agree rather well with the observations except about $\approx$ 3 MeV where they are smaller than the measured values. The difference lies in the CN contribution from the continuum of levels. This was calculated using the the statistical formalism of ref. [GC65], as applicable to ^{118}Sn. There appears to be too much CN channel competition from the continuum of levels. The result is very sensitive to the assumed statistical temperature (T), and the discrepancy can be removed with a relatively

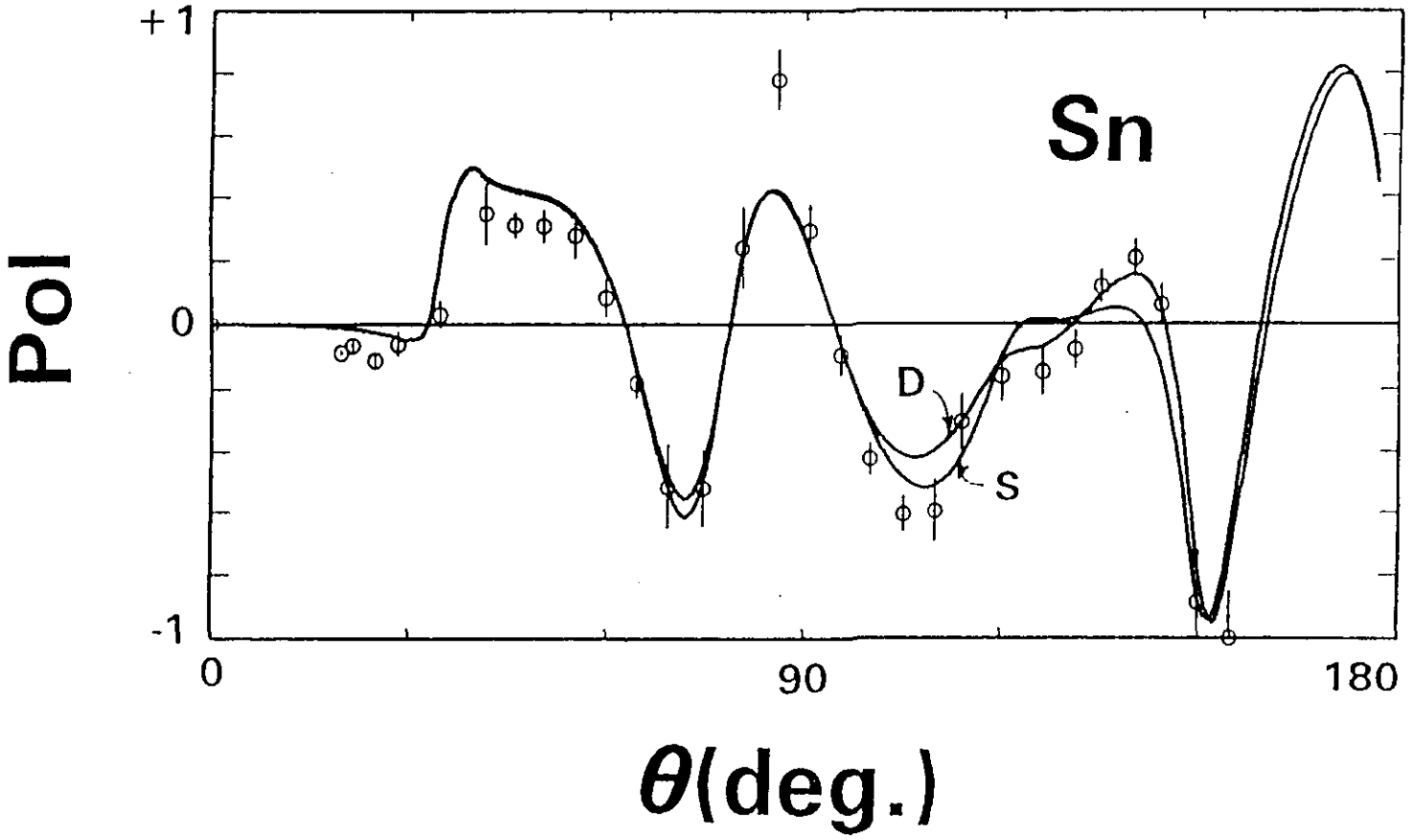

Fig. 5.4.1. Measured (symbols) and calculated (curves) polarizations of 10 MeV neutrons elastically scattered from ^{120}Sn. The measured values were taken from ref. [Gus+89]. The "S" curve was obtained using the ESOM and the "D" curve using the CCM.

small increase in T, as was verified at several incident energies.

The calculated excitations of the observed elemental level at $\approx$ 2.27 MeV are very much dominated by the contributions of the 3^- level. They (the lower curve of the relevant portion of Fig. 3.3.2) are consistently smaller than the measured values. If β_3 is increased to 0.180 the calculated result is still smaller than the measured values (the upper curve in Fig. 3.3.2). The difference between measured and calculated values is not large and probably reflects a number of small contributions to the measured values from other levels not considered in the calculations. Such a trend should be expected.

The β_2 used above was taken from the EM values [Ram+87], but the interaction strength depends upon the deformation length $\delta_i = r_v \cdot \beta_i$, and throughout the range of the present measurements r_v is both energy dependent and significantly larger than the 1.2 fm conventionally used in EM considerations. Thus the β_2 used in the calculations should increase with energy in the region of the present experiments. Such an effect is obscured by the elemental nature of the data base and by the onset of uncertain CN calculations.

The above elemental considerations can be extended and the model further benchmarked using isotopic inelastic-scattering information found in the literature ([Gus+89], [Fin+80A], [Chi+88]). The experimental results of Guss et al. [Gus+89] and Findlay et al. [Fin+80A] appear to be of excellent quality. The latter are of wide isotopic scope including the major even isotopes $^{116\text{-}124}$Sn. The optimum incident energy appears to $\approx$ 11 MeV where the CN contributions are negligible and possible volume absorption is not yet a concern. The CCM of Table 4.5.1 was used to calculated the differential inelastic scattering cross sections for the excitation of the yrast (2^+) level at 11 MeV using β_2 = 0.08, = 0.10 and = 0.12. The calculated results are compared with the experimental values of ref. [Fin+80A] in Fig. 5.5.1. There are detailed discrepancies between measured and calculated values but, generally, the calculated values follow the angular-dependent shapes of the measured distributions. It is also evident that β_2 decreases with mass (as is expected with the filling of the neutron shell), indicating an asymmetry ($\frac{N-Z}{A} = \eta$) dependence of the form $\beta_2 = \beta_2^o \cdot (1 - \xi_2 \cdot \eta)$. With this assumption the 11 MeV isotopic results of ref. [Fin+80A] were fitted using the CCM potential of Table 4.5.1, varying β_2 to obtain a chi-square minimum. This fitting resulted in a $\beta_2 = 0.157 \cdot (1 - 2.22 \cdot \eta)$ and $\delta_2 = 0.91 \cdot (1 - 2.09 \cdot \eta)$. These values are to be compared with $\beta_2 = 0.164 \cdot (1 - 2.19 \cdot \eta)$ and $\delta_2 = 0.93 \cdot (1 - 2.02 \cdot \eta)$ resulting from the work of refs. [Fin+80A] and [Fin+80B]. Though limited to considerations of

^{116}Sn and ^{120}Sn, the results of ref. [Gus+89] lead to $\delta_2 = 0.914\cdot(1-2.01\cdot\eta)$. The agreement between the various results is remarkably good. This is in part due to the fact that the same data base was employed in the present work and that of ref. [Fin+80A], but the potentials used were entirely independent and the work of refs. [Fin+80A] and [Fin+80B] employed DWBA methods while the present work uses the CCM approach. In refs. [Fin+79] and [Fin+80A] comparisons were made with (p,p') studies of the same isotopes reported in refs. [Bee+70] and [Mak+68], with average results of $\beta_2 = 0.195\cdot(1-2.26\cdot\eta)$ and $\delta_2 = 1.110\cdot(1-2.08\cdot\eta)$. Similar comparisons can be made with the EM values deduced from coulomb-excitation measurements [Ram+87]. The latter yield $\beta_2 = 0.15\cdot(1-1.86\cdot\eta)$ and $\delta_2 = 0.87\cdot(1-1.67\cdot\eta)$. It is clear that the asymmetry dependencies of the δ_2 values obtained from (n,n') and (p,p') measurements is in remarkably good agreement, and the EM equivalent is probably significantly smaller. It is also apparent that $\delta_2(p,p') > \delta_2(n,n') > \delta_2(EM)$. This is consistent with the theoretical predictions of the core-polarization model of Brown and Madsen [BM75]. However, one should not construe that $\delta_2(p,p') > \delta_2(n,n')$ in a global context as tin is magic in proton number, Z = 50, and it is known ([Bai+78], [BM75]) that the relationship is inverted in the N = 50 region.

Comparisons such as the above can be made at other energies. They are probably most productive in the context of ^{116}Sn as detailed differential cross sections for the excitation of the yrast (2^+) level are available at 10 and 14 MeV from the work of Guss et al. [Gus+89] and at 11 and 24 MeV from the work of Finlay et al. [Fin+80A]. These results are compared with values calculated with the potential of Table 4.5.1 in Fig. 5.5.2. The agreement between measured and calculated results is reasonably good except at 14 MeV where the measured values appear anomalously large at forward scattering angles. Calculations reported in the literature specifically addressing these cross sections ([Gus+89], [Fin+80A]) gave essentially the same results, and had the same problem with the 14 MeV data at forward angles. At 10 and 11 MeV the β_2 is approximately 0.113 following from the chi-square fitting discussed above. It is uncertain at 14 MeV due to the scatter of the data, and appears to be in the range 0.14 to 0.16 at 24 MeV. These results suggest a rather large increase in β_2 with energy. About a third of it is due to the energy dependence of the radius as it is δ_2 that should be compared. At 24 MeV the CCM may well be at the upper limit of its range of validity, the fitting used in deducing the model was not outstanding at 24 MeV (chi-squares were larger), and at the higher energies the coupling schemes may be more complex than assumed in the model. These factors may well contribute to what appears to be a rather sharp energy dependence of the δ_2

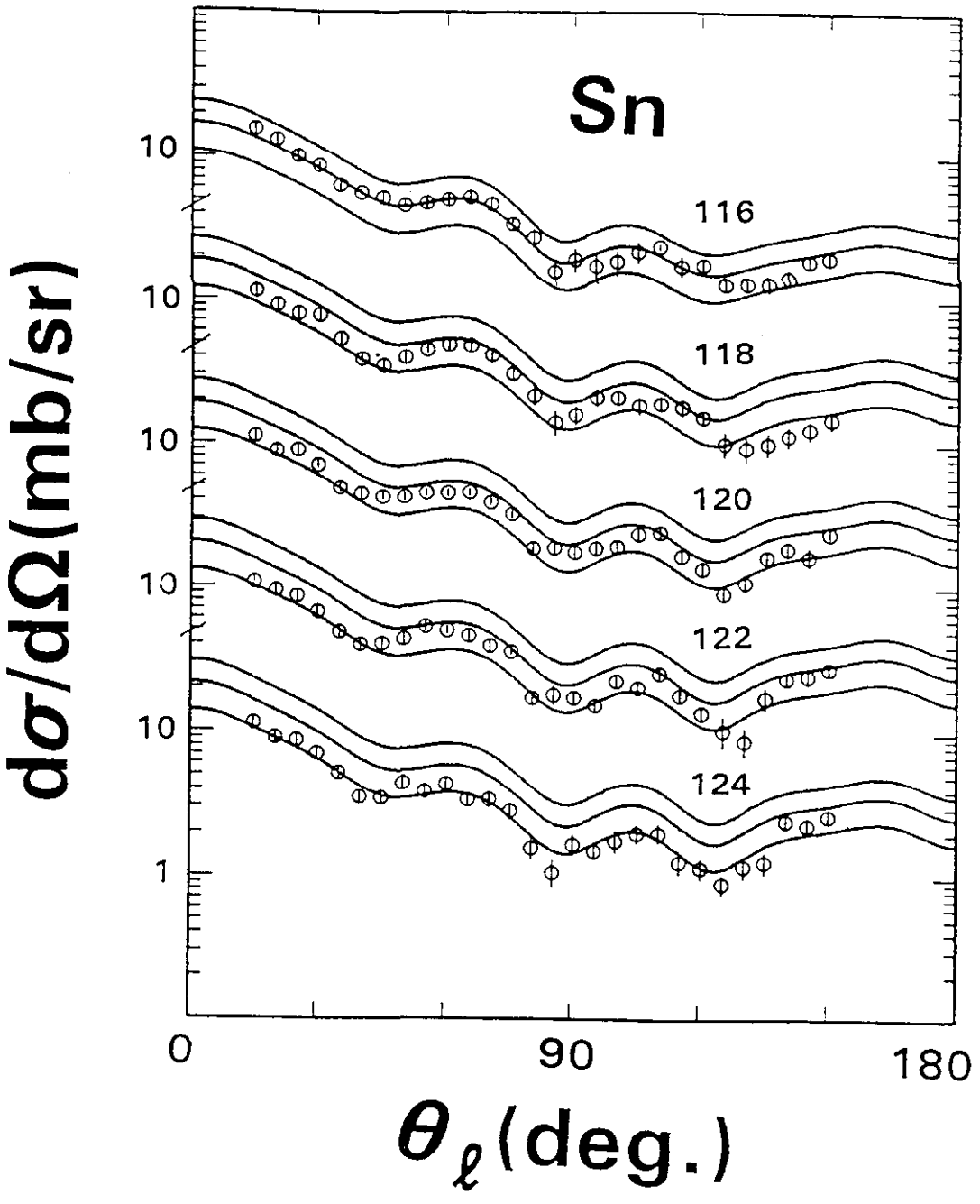

Fig. 5.5.1. Comparisons of measured (symbols) [Fin+80A] and calculated (curves) differential cross sections for the excitation of the yrast (2^+) levels in $^{116\text{-}124}$Sn at 11 MeV. Three curves are shown for each isotope corresponding to β_2 = 0.08 (lower), = 0.10 (mid) and = 0.12 (upper). The isotopes are numerically noted.

implied in Fig. 5.5.2. Global models indicate that δ_2 is only slowly changing with energy, if at all.

The above ^{116}Sn comparisons can be extended to the 3^- level at 2.266 MeV using the data of refs. [Gus+89] and [Fin+80A]. Again, the calculations employed the potential of Table 4.5.1 in the manner outlined above in the context of angle-integrated cross sections. The calculated results were reasonably consistent with the measured values as shown in Fig. 5.5.3. Similar calculations explicitly directed toward these cross sections (e.g., Gus+89]) gave essentially the same quality of results. Again, there is some tendency for the 24 MeV distribution to suggest increasing β_3 values compared to the lower-energy results. The comparisons are compromised as several other states contribute to the measurements and they were not addressed in the calculations. However, the calculations indicate that by far the primary component of the cross sections is due to the 3^- level. An interpretation of the neutron inelastic scattering data in ref. [Fin+80A] leads to $\delta_3 = 1.79\cdot(1-2.83\cdot\eta)$ with a similar expression derived from proton-scattering data. However, it was necessary to make subjective judgment as to the effect of experimental resolution in the neutron measurements so the effort was not repeated here. Most of the cross sections primarily due to the direct excitation of the 3^- level (and associated levels) are small, and the discrepancies between measured and calculated values are of the order of a mb and thus not of applied interest.

5.6. Isospin Effects

As noted above, isoscaler and isovector strengths are treated in terms of volume-integrals-per-nucleon, J_i. In a narrow mass range J_i are good indexes of strength, but over a wide mass range there will be significant distortions that approximately double the relative isovector strengths (e.g., see refs. [HW68] and [Fer+77]).

In the present tin case the mass range is relatively narrow but even in this scope there is a considerable scatter of isoscaler and isovector strengths deduced from (p,p) and (n,n) studies as illustrated in Table 5.6.1. The present ESOM, DOM and CCM real strengths are quite consistent, with a mean asymmetry dependence given by $J_v = 430\cdot(1-0.45\cdot\eta)$. This result is in reasonable agreement with theoretical estimates based upon nucleon-nucleon scattering which suggest $J_v = J_0\cdot(1-0.48\cdot\eta)$ ([TSW63], [OP66], [TT67], [GPT68] and [GMP70]). It is also consistent with a number of experimental results deduced from both (n,n) and (p,p) measurements. The agreement of the J_w representations of the present work is acceptable (remembering that J_{wo} of the CCM will be smaller due to the explicit level treatment).

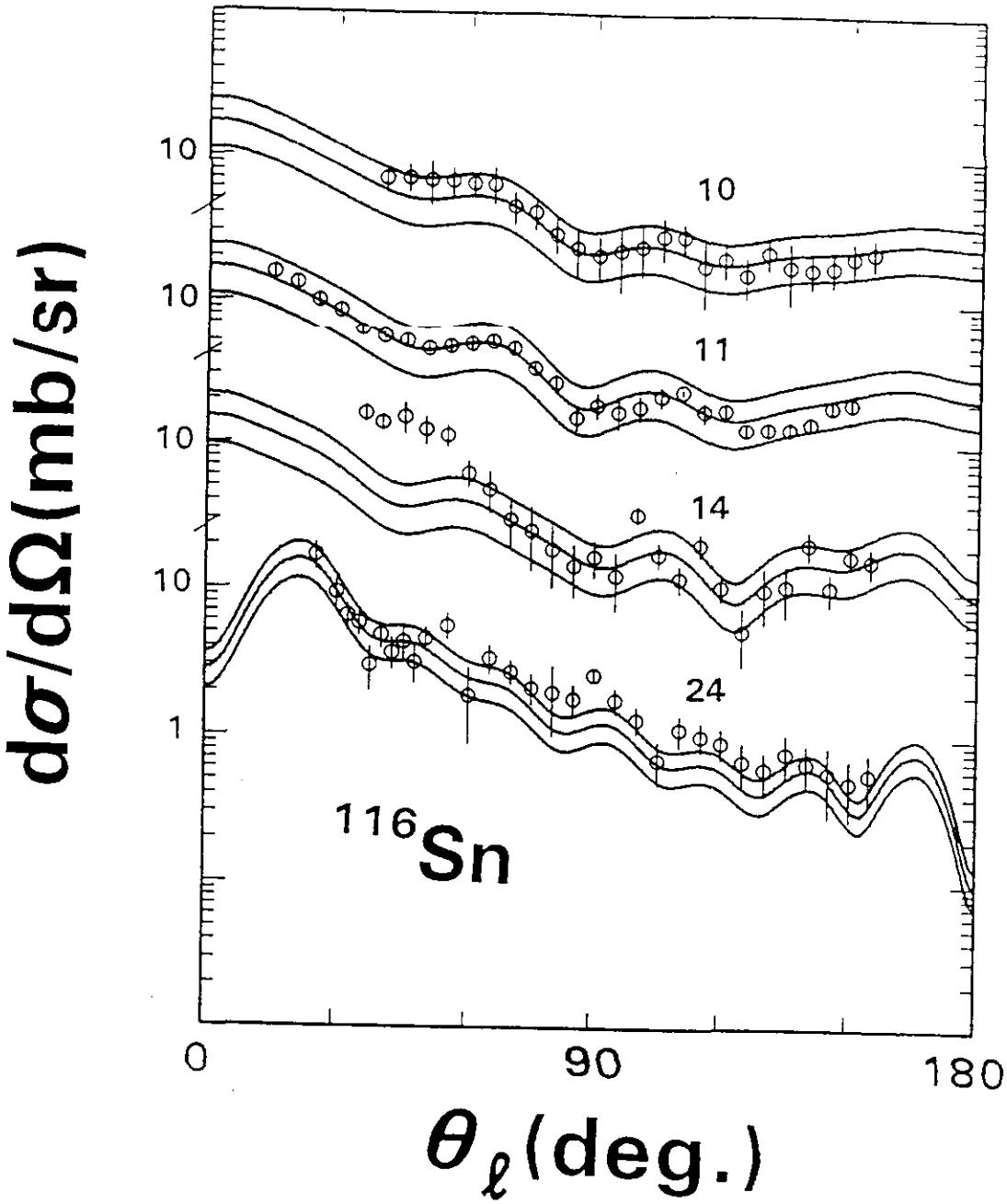

Fig. 5.5.2. Differential cross sections for the excitation of the yrast (2^+) state in ^{116}Sn at 10, 11, 14 and 24 MeV. Measured data taken from refs. [Gus+89] and [Fin+80A] are indicated by symbols. Curves indicate the results of calculations as described in the text. There are three calculated distributions at each energy, corresponding to β_2 = 0.08, = 0.10 and = 0.12 at 10 → 14 MeV, and = 0.12, = 0.14 and = 0.16 at 24 MeV. Incident energies are numerically noted.

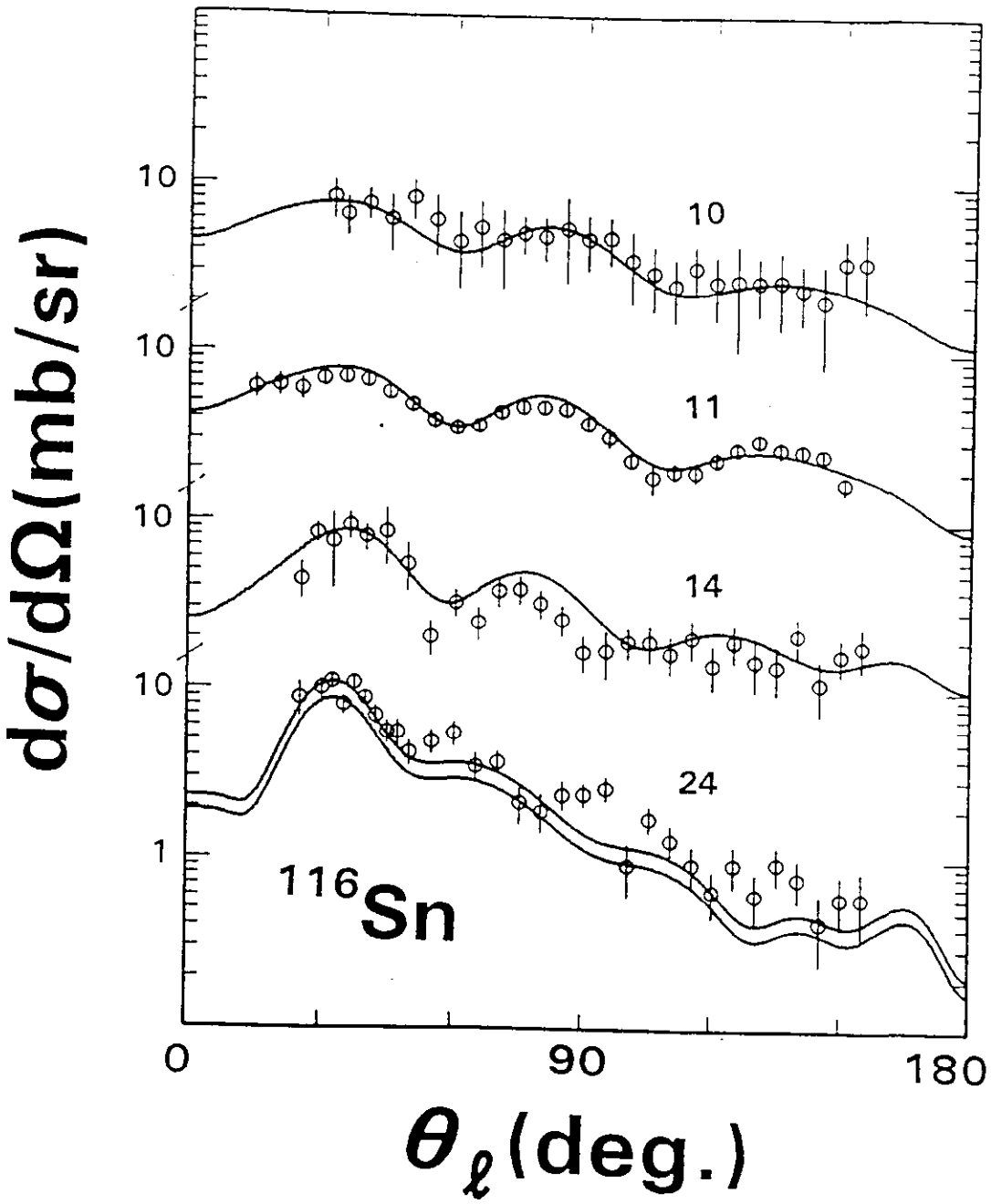

Fig. 5.5.3. Measured and calculated cross sections for the excitation of the 2.266 (3^-) MeV level in ^{116}Sn. Measured values from refs. [Gus+89] and [Fin+80A] are indicated by symbols. Curves correspond to calculations with $\beta_2 = 0.10$ and $\beta_3 = 0.16$, with the addition of a curve at 24 MeV using $\beta_3 = 0.18$. Incident energies are numerically given in MeV.

Corresponding values found in the literature scatter by large amounts in many cases and are uncertain in others due to volume absorption. Most "global" models represent the relative isovector strength as approximately energy independent while there is some suggestion from the present interpretations that the relative isovector/isoscaler strength decreases with energy. That result is very uncertain as the data is not definitive above 11 MeV. As outlined above, there was no justification to accept anything but the simple $R_i = r_i \cdot A^{1/3}$ radial dependence on mass. Throughout the present work it was assumed that the isoscaler and isovector potentials had the same SW shape. That is the commonly-used assumption but it is not necessarily true [Sat69]. Indeed, the radius of the neutron density distribution is probably greater than that of the protons by ≈ 0.6 fm, thus one might suspect that the isovector contribution to the potential might be more focused upon the surface ([BG68], [GPT68]). Some attempts to investigate such an eventuality in the present work were not successful. Finally, one should remember that the tin isotopes are magic in proton number, $Z = 50$, and that it is known that there is an inversion of the imaginary-potential isovector contribution to the potential near $N = 50$ ([Rap+79A], [Chi+90]). Thus it may be risky to extrapolate the present isoscaler and isovector behavior over a much wider mass scope.

5.7. The Bound Regime

The even isotopes of tin have a closed proton shell, and one can expect the neutron single-particle states to be in the $2d_{5/2}$, $1g_{7/2}$, $3s_{1/2}$, $2d_{3/2}$ and $1h_{11/2}$ orbits. It is known [LGS87] that the primary impact of the dispersion integral is at bound energies. The particle states can be used to test the present models into the bound-energy regime of the shell model. ^{118}Sn was selected for this purpose as its mass is nearest that of the elemental data primarily used in deriving the present potentials. Several (d,p) studies have reported single-particle states in ^{118}Sn (c.g., see refs. [Bor+75], [CP61] and [Sch+67]). The most recent work appears to be that of Borello-Lewin et al. [Bor+75] which reports binding energies for the $2d_{5/2}$, $1g_{7/2}$, $3s_{1/2}$, $1h_{11/2}$ and $2d_{3/2}$ single-particle states (and gives a lower limit for the $2f_{7/2}$ state). These binding energies are rather closely clumped about the fermi energy. Therefore the dispersion integral of Eq. 4.4.1 should have a relatively small effect and the ESOM of Table 4.3.3 can be reasonably used to estimate the binding energies near the fermi surface. Comparative results are shown in Table 5.7.1. The calculated results for the four deepest-bound states are quite consistent with the measured values. That for the $2d_{3/2}$ state is not consistent with the experimental values of ref. [Bor+75]. However, there is an uncertainty in this case, and the relative experimental results of ref. [Sch+67] suggest a binding energy much closer to the calculated value. Ref. [Bor+75] also gives a lower limit for the

Table 5.6.1. Real and imaginary isoscalar and isovector strengths of tin (in volume-integrals-per-nucleon, MeV-fm^3) expressed in the form $J_i = J_{io}\cdot(1-C\cdot\eta)$ where $\eta \equiv (N-Z)/A$. All values refer to the (n,n) reaction at 11 MeV unless otherwise stated. It is assumed that the radius has the $R \equiv r\cdot A^{1/3}$ mass dependence and that the isoscalar and isovector potentials have the same SW geometry.

Reference	J_{real}	J_{imag}
Present Work		
ESOM	$432\cdot(1-0.45\cdot\eta)$	$103.5\cdot(1-1.81\cdot\eta)$
DOM	$430\cdot(1-0.44\cdot\eta)$	$100.6\cdot(1-1.84\cdot\eta)$
CCM	$428\cdot(1-0.45\cdot\eta)$	$89.6\cdot(1-1.73\cdot\eta)$
[Won+84] (n,n), (p,p) and (p,n) reactions	$417\cdot(1-0.52\cdot\eta)$	$89.4\cdot(1-1.41\cdot\eta)$
[Mak+68] (p,p) at 16 MeV. * Omit ^{112}Sn	$407\cdot(1-0.37\cdot\eta)^*$	$95.4\cdot(1+1.83\cdot\eta)^*$
[Har+84]		
At 1.0 MeV	$479\cdot(1-0.57\cdot\eta)$	$95.5\cdot(1-3.56\cdot\eta)$
at 1.6 MeV	$471\cdot(1-0.60\cdot\eta)$	$78.0\cdot(1-2.93\cdot\eta)$
[Fer+77] Table 4 of ref.	$438\cdot(1-0.49\cdot\eta)$	$94.4\cdot(1-1.08\cdot\eta)$
[Gus+89] CCM	$437\cdot(1-0.49\cdot\eta)$	$83.1\cdot(1-1.99\cdot\eta)$
[Rap+79]		
11 MeV	$415\cdot(1-0.48\cdot\eta)$	$91.1\cdot(1-1.48\cdot\eta)$
24 MeV	$380\cdot(1-0.47\cdot\eta)$	---
Use Pot. "A"		
[Rap+80]	$415\cdot(1-0.41\cdot\eta)$	$100.0\cdot(1-1.84\cdot\eta)$
[Fer+76] (n,n) and (p,p) comparisons	$449\cdot(1-0.39\cdot\eta)$	$102.0\cdot(1-0.98\cdot\eta)$

Table 5.6.1, Continued

[HW68] Wide mass range at 8 MeV	$470 \cdot (1-0.85 \cdot \eta)$	----------
[Bee+70] (p,p) at 24 MeV, omit ^{118}Sn	$375 \cdot (1+0.51 \cdot \eta)$	$112.0 \cdot (1+1.17 \cdot \eta)$
[Fin+80B] Use Table 2	$414 \cdot (1-0.40 \cdot \eta)$	$99.8 \cdot (1-1.85 \cdot \eta)$
[BG69]	$414 \cdot (1-0.56 \cdot \eta)$	----------

binding energy of the $2f_{7/2}$ level of $\approx$ 3.9 MeV which is consistent with the ESOM calculated value of 2.1 MeV. Generally, these binding-energy comparisons give support to the ESOM potential of Table 4.3.3 which was obtained entirely from the unbound neutron data. The differences between calculated and measured values tend to be less than those between various (d,p) experimental results and there will be small adjustments in the calculated values due to dispersion effects. Stringent tests of latter would require experimental results further from the fermi energy.

Acknowledgements

The author is very appreciative of the contributions made by Drs. C. Budtz-Jorgensen, P. T. Guenther and S. Chiba in the early portions of this work.

Table 5.7.1. Comparison of experimental and calculated single-particle binding energies in ^{118}Sn. The calculations used the ESOM potential as discussed in the text.

	Binding Energies (MeV)				
State	$2d_{5/2}$	$1g_{7/2}$	$3s_{1/2}$	$1h_{11/2}$	$2d_{3/2}$
Experiment	10.9[a]	9.5[a]	8.5[a]	7.4[a]	6.8[a]
					$\approx$ 8.1[b]
ESOM Cal.	10.9	9.8	8.8	7.3	8.5

[a] Ref. [Bor+75].
[b] Ref. [Sch+67].

REFERENCES

[Bai+78] D. E. Bainum, R. W. Finlay, J. Rapaport, M. H. Hadizadek and J. D. Carlson, Nucl. Phys. A311 492 (1978).

[Bau+82] M. Bauer, E. Hernandez-Saldana, P. E. Hodgson and J. Quintalinlla, J. Phys. G8 525 (1982).

[Bee+70] O. Beer, A. El Behay, P. Lopato, Y. Terrien, G. Vallois and K. K. Seth, Nucl. Phys. A147 326 (1970).

[BG68] R. N. Boyd and G. W. Greenlees, Phys. Rev. 176 1394 (1968).

[BG69] F. D. Becchetti Jr. and G. W. Greenlees, Phys. Rev. 182 1190 (1969).

[BGS82] C. Budtz-Jorgensen, P. T. Guenther and A. B. Smith, Argonne National Laboratory Report, ANL/NDM-73 (1982).

[BM75] V. R. Brown and V. A. Madsen, Phys. Rev. C11 1298 (1975); also Phys. Rev. Lett. 34 1388 (1975) and Phys. Rev. C12 1205 (1975).

[Bor+75] T. Borello-Lewin, C. Q. Orsini, O. Dietzsch and E. W. Hamburger, Nucl. Phys. A249 284 (1975).

[BR78] F. A. Brieva and J. R. Rook, Nucl. Phys. A307 493 (1978).

[Chi+88] S. Chiba et al., Nucl. Sci. and Tech. (Japan) 25 511 (1988).

[Chi+90] S. Chiba, P. T. Guenther, R. D. Lawson and A. B. Smith, Phys. Rev. C42 2487 (1990).

[CL55] L. Cranberg and J. Levin, Proc. Inter. Conf. on Peaceful Uses of Atomic Energy (United Nations Press, New York, 1955).

[CP61] B. L. Cohen and R. E. Price, Phys. Rev. 121 1441 (1961).

[CL56] L. Cranberg and J. S. Levin, Phys. Rev. 103 343 (1956).

[CSL83] Nuclear Standards File, IAEA Tech Report 227, eds. H. Conde, A. Smith and A. Lorenz (1983).

[Del+83] J. P. Delaroche, P. P. Guss, C. E. Floyd, R. L. Walter and W. Tornow, Phys. Rev. C27 2385 (1983).

[Dro87] M. Drosg, IAEA Report, IAEA-TECDOC-410 (1987).

[ENDF] Evaluated Nuclear Data File/B, Version VI, Available from the National Nuclear Data Center, Brookhaven National Laboratory.

[Fer+76] J. C. Ferrer, J. D. Carlson and J. Rapaport, Phys. Lett. 62B 399 (1976).

[Fer+77] J. C. Ferrer, J. D. Carlson and J. Rapaport, Nucl. Phys. A275 325 (1977).

[FG71] D. Foster and D. Glasgow, Phys. Rev. C3 576 (1971).

[Fin+79] R. W. Finlay, J. Rapaport, V. R. Brown, V. A. Madsen and J. R. Comfort, Phys. Lett. 84B 169 (1979).

[Fin+80A] R. W. Finlay, M. H. Hadizadeh, J. Rapaport and D. E. Bainum, Nucl. Phys. A344 257 (1980).

[Fin+80B] R. W. Finlay, J. Rapaport, M. H, Hadizadeh, M.Mirzaa and D. E. Bainum, Nucl. Phys. A338 45 (1980).

[Fin+93] R. W. Finlay, W. P. Abfalterer, G. Fink, E. Montei, T. Adami, P. W. Lisowski, G. L. Morgan and R. C. Haight, Phys. Rev. C47 237 (1993).

[GC65] A. Gilbert and A. Cameron, Can. J. Phys. 43 1446 (1965).
[GMP70] G. W. Greenlees, W. Makofske and G. J. Pyle, Phys. Rev. C1 1145 (1970).
[GPT68] G. W. Greenlees, G. J. Pyle and Y. C. Tang, Phys. Rev. 171 1115 (1968).
[Gus+89] P. P. Guss, R. C. Byrd, C. R. Howell, R. S. Pedroni, G. Tungate, R. L. Walter and J. P. Delaroche, Phys. Rev. C39 405 (1989).
[Har+84] R. W. Harper, J. L. Weil and J. D. Brandenberger, Phys. Rev. C30 1454 (1984).
[HF52] W. Hauser and H. Feshbach, Phys. Rev. 87 362 (1952).
[HW68] B. Holmqvist and T. Wiedling, Phys. Lett. 27B 411 (1968); also see Nucl. Phys. A188 24 (1972).
[Hod71] P. E. Hodgson, Nuclear Reactions and Nuclear Structure (Clarendon, Oxford, 1971).
[JLM76] J. P. Jeukenne, A. Lejeune and C. Mahaux, Phys. Reports C25 83 (1976),
[Lan62] A. M. Lane, Phys. Rev. Lett. 8 171 (1962); Nucl. Phys. 35 676 (1962).
[LHH81] D. Larson, J. Harvey and N. Hill, Oakridge National Laboratory Report, ORNL-5878 (1981).
[LGS87] R. D. Lawson, P. T. Guenther and A. B. Smith, Phys. Rev. C36 1298 (1987).
[Mak+68] W. Makofske, W. Savin, H. Ogata and T. H. Kruse, Phys. Rev. 174 1429 (1968).
[MDH81] S. Mughabghab, M. Divadeenam and N. Holden, Neutron Cross Sections (Academic, New York, 1971).
[Mey73] W. D. Meyers, Nucl. Phys. A204 465 (1973).
[MN82] C. Mahaux and N. Ngo, Nucl. Phys. A378 205 (1982); also Phys. Lett. B100 285 (1981).
[Mol63] P. A. Moldauer, Nucl. Phys. 47 63 (1963).
[Mol80] P. A. Moldauer, Nucl. Phys. A344 185 (1980).
[Mol81] P. A. Moldauer, The coupled-channels computer code ANLECIS, private communication (1981); a modification of the ECIS code of J. Raynal, NEA memorandum (1979).
[Mol82] P. A. Moldauer, Spherical optical-model code ABAREX, private communication (1982); modified by S. Chiba for elemental use.
[MW66] J. Meadows and J. Whalen, Argonne National Laboratory Report, ANL-7210 (1966).
[Nak+86] Y. Nakajima, M. Ohkubo, Y. Furuta, M. Sugimoto and Y. Kawarsaki, Proc. Conf. on Nucl. Data for Basic and Applied Science, eds. P. Young et al. (Gordon and Breach, New York, 1986) vol. 1, p. 947.
[NDC72] C. M. Newstead, J. P. Delaroche and B. Cauvin, Statistical Properties of Nuclei (Plenum, New York, 1972) p. 367.

[NDS] L. K. Pekar, Nucl. Data Sheets 29 587 (1980); J. Blachot and G. Marguier, Nucl. Data Sheets 35 375 (1982); B. Harmatz, Nucl. Data Sheets 30 413 (1980); J. Blachot, J. P. Husson, J. Oms, G. Marguier and F. Haas, Nucl. Data Sheets 32 287 (1981); J. Blachot and G. Marguier, Nucl. Data Sheets 50 63 (1987); T. Tamura, K. Miyano and S. Ohya, Nucl. Data Sheets 51 259 (1987); R. L. Auble, Nucl. Data Sheets 26 207 (1979); D. C. Kocher, Nucl. Data Sheets 17 39 (1976); K. Kitao, M. Kanbe, Z. Matsumoto and T. Seo, Nucl. Data Sheets 49 315 (1986); T. Tamura, K. Mikano and S. Ohya, Nucl. Data Sheets 41 413 (1984).

[OP66] S. Oaki and S. C. Park, Phys. Rev. 145 787 (1966).

[Pat+76] D. M. Patterson, R. R. Doering and A. Galonski, Nucl. Phys. A263 261 (1976).

[PS86] A. B. Popov and G. S. Samosuat, Proc. Conf. on Nucl. Data for Basic and Applied Science, eds. P. Young et al. (Gordon and Breach, New York, 1986) vol. 1, p. 621.

[PW83] W. P. Poenitz and J. F. Whalen, Argonne National Laboratory Report, ANL/NDM-80 (1983).

[PWS81] W. Poenitz, J. Whalen and A. Smith, Nucl. Sci. and Eng. 78 333 (1981).

[Ram+87] S. Raman, C. H. Malarkey, W. T. Miller, C. W. Nester Jr. and P. H. Stelson, At. Data and Nucl. Data Tables 36 1 (1987).

[Rap+79] J. Rapaport, V. Kulkarni and R. W. Finlay, Nucl. Phys. A330 15 (1979).

[Rap+79A] J. Rapaport, T. S. Cheema, D. E. Bainum, R. W. Finlay and J. D. Carlson, Nucl. Phys. A313 1 (1979).

[Rap+80] J. Rapaport, M. Mirzaa, M. Hadizadeh, D. E. Bainum and R. W. Finlay, Nucl. Phys. A341 56 (1980).

[Sat69] G. R. Satchler, Isospin in Nuclear Physics ed. D. H. Wilkinson (North-Holland, Amsterdam, 1969) p. 389.

[Sat83] G. R. Satchler, Direct Nuclear Reaction (Clarendon, Oxford, 1983).

[Sch+67] E. J. Schneid, A. Prakash and B. L. Cohen, Phys. Rev. 156 1316 (1967).

[SGS77] A. Smith, P. Guenther and R. Sjoblum, Nucl. Instr. and Methods 140 397 (1977).

[SH67] A. Smith and R. Hayes, Nucl. Phys. A93 607 (1967).

[Sha63] C. Shakin, Ann. Phys. (New York) 22 373 (1963).

[Smi90] A. B. Smith, Argonne National Laboratory memorandum, unpublished (1990).

[Smi+92] A. B. Smith and P. T. Guenther, Argonne National Laboratory Report, ANL/NDM-127 (1992); S. Chiba, P. Guenther, A. Smith, M. Sugimoto and R. Lawson, Phys. Rev. C45 1260 (1992); C. Budtz-Jorgensen, P. Guenther, A. Smith and J. Whalen, Z. Phys. A306 265 (1982); and references cited therein.

[Ste+65] P. Stelson, R. L. Robinson, H. J. Kim, J. Rapaport and G. R. Satchler, Nucl. Phys. 68 97 (1965).

[Tan+71] S. Tanaka et al., NEA Report, EANDC(J)-22 (1971).

[Tan+72] S. Tanaka et al., Budapest Conf. (1972), data available from the National Nuclear Data Center.

[TC88] C. E. Till and Y. I. Chang, Advances in Nucl. Sci. and Technology, 20 127 (1988).

[TSW63] Y. C. Tang. E. Schmid and K. Wildermuth, Phys. Rev. 131 2631 (1963).

[TT67] D. R. Thompson and Y. C. Tang, Phys. Rev. 159 806 (1967).

[WG86] R. L. Walter and P. P. Guss, Proc. Conf. on Nucl. Data for Basic and Applied Science, eds. P. Young et al. (Gordon and Breach, New York,1986) vol. 2, p. 1079.

[WH64] D. Wilmore and P. E. Hodgson, Nucl. Phys. 55 673 (1964).

[Won+84] C. Wong, S. M. Grimes and R. W. Finlay, Phys. Rev. C29 1710 (1984).